NTNU – Trondheim
Norwegian University of
Science and Technology

SAG-FW Welding of C90 Riser Steel Connectors

Aleksander Rudolf Stoss

Materials Science and Engineering
Submission date: June 2012
Supervisor: Jan Ketil Solberg, IMTE
Co-supervisor: Bjarne Salberg, AMR

Norwegian University of Science and Technology
Department of Materials Science and Engineering

i Abstract

Weld simulations have been conducted on a C90 quenched tempered steel used in offshore riser systems, in order to investigate the possibility of introducing an effective solid state weld procedure. As a secondary objective, the microstructure of the HAZ of a TIG welding is to be evaluated. The C90 is as steel of high hardenability and its base microstructure consists of tempered *martensite* with a Vickers hardness of 239 HV10. The main focus in this work has been to sufficiently soften the weld as well as obtaining impact toughness properties within requirements, by implying a post weld heat treatment procedure. Hardness values cannot exceed 270 HV10 and impact toughness energy must exhibit an average value above 40 J. Steel samples have been heated to a peak temperature of 1150 ˚C, followed by controlled cooling at 10 and 60 ˚C/s, prior to post weld heat treatment. Tempering at temperatures of 680 and 720 ˚C has been conducted on the post quenched structure for up to three hours and has been performed in an air circulating furnace and in a Smitweld Thermal Cycle apparatus. Low tempering times (up to 1200 s) have been performed in the Smitweld apparatus. Weld hardness and impact toughness requirements was met after three hours of post weld heat treatment at 720 ˚C in an air circulating furnace, producing a hardness value of 253 HV10 and a Charpy-V energy of 66 J for the parallel quenched at 10 ˚C/s. After some tempering of the structure, the two cooling rates used did not affect hardness values significantly. Tempering at 680 ˚C did not soften the structure sufficiently to meet the criteria, with the lowest measured hardness of 315 HV10 after three hours. The hardness of the intercrictial zone of the weld was reduced to 246 HV10 after tempering for three hours at 720 ˚C. Tempering in the Smitweld apparatus softened the structure more efficiently than what was observed in the furnace, producing hardness values of 271 HV10 after only twenty minutes of tempering at 720 ˚C. It has been suggested that due to substantially higher heating rates obtained by the Smitweld apparatus, low temperature tempering mechanisms may be inhibited or delayed, resulting in a post tempered structure consisting of coarse carbides with large inter particle spacing, contributing little to precipitation hardening. Heating rates obtained by Smitweld is in the same range as those obtainable by the SAG-FW procedure, and the two methods are therefore considered comparable. FMC Technologies uses a TIG weld procedure followed by a six hour post weld heat treatment to obtain satisfactory mechanical properties on the C90 steel quality. It is suggested, that by applying a solid state weld procedure, the total tempering time can be reduced with at least 50 %.

ii Sammendrag

Sveisesimulering har blitt utført på et C90 QT stål som brukes i offshore riser systemer, for å undersøke muligheten for sammenføyning ved bruk av en smisveise prosedyre (SAG-FW). C90 stålkvaliteten har høy herdbarhet og utgangsstrukturen består av anløpt martensitt med en Vickers hardhetsverdi på 239 HV10. Hovedfokuset i denne oppgaven har vært å mykne sveisen tilstrekkelig ved å innføre en passende varmebehandlingsprosedyre, samt å oppnå tilfredsstillende slagseighetsverdier. Hardhetsverdier kan ikke overstige 270 HV10 og gjennomsnittlig slagseighetsenergi må være over 40 J. Stålprøver har blitt varmet til 1150 ˚C for så å bli kontrollert avkjølt med 10 og 60 ˚C/s før de har blitt eksponert for varmebehandling i opptil tre timer ved 680 og 720 ˚C. Varmebehandlingen har blitt utført i både en Smitweld Thermal Cycle simulator og i luftsirkulert ovn. Anløpingstider opptil 1200 sekunder har blitt utført i Smitweld apparaturen. Etter tre timers ovnsanløpning ved 720 ˚C ble tilfredsstillende hardhet og slagseighetsverdier målt til 253 HV10 og 66 J for parallellen avkjølt med 10 ˚C/s. Avkjølingsratene brukt i dette arbeidet, påvirket i liten grad forskjell i hardhetsverdier etter at strukturen var blitt varmebehandlet. Prøver anløpt i tre timer ved 680 ˚C oppnådde ikke hardhetsverdier innenfor kravene. Hardhet av interkritisk sone ble redusert til 246 HV10 etter tre timers anløpning ved 720 ˚C. Varmebehandling i Smitweld apparaturen reduserte hardheten i strukturen mer effektivt enn det observert ved ovnsanløpning, og hardhetsverdier på 271 HV10 ble oppnådd etter kun 20 minutters anløpning. Det er foreslått, at den raske oppvarmingen av stålemnet i Smitweld apparaturen sammenlignet med ovnsanløpning, hemmer eller forsinker anløpningsmekanismer ved lave temperaturer noe som medfører at strukturen etter anløpning inneholder få store karbider, grovt distribuert i den anløpte martensitten slik at de bidrar lite til presipitatherding. Smitweld apparaturen og SAG-FW prosessen opererer begge med oppvarmingsrater i det samme området, og disse to metodene er derfor ansett som sammenlignbare. FMC Technologies benytter en TIG sveiseprosedyre fulgt av en seks timer lang anløpningssekvens for å oppnå tilfredsstillende mekaniske egenskaper for C90 stålkvaliteten. Det er foreslått med bakgrunn i dette arbeidet, at den totale anløpningstiden kan reduseres med minst 50 % ved å benytte en smisveiseprosedyre i stedet for konvensjonell TIG med påfølgende varmebehandling.

iii Acknowledgements

I wish to express my gratitude to the people who have helped and supported me during the completion of this work.

I am grateful for the guidance and support from my supervisor Prof. Jan Ketil Solberg and co-supervisor Bjarne Salberg, which have always been available for discussions and consultations. I owe a special gratitude to Per Thomas Moe for his involvement in this work and for evaluating my progress.

Table of contents

List of figures

List of tables

List of abbreviations and symbols

Ac	Transformation temperature upon heating
$Ac_{,0.03}$	Observed transformation temperature upon heating at 0.03 ˚C/s
$Ac_{,160}$	Observed transformation temperature upon heating at 160 ˚C/s
Ae	Transformation temperature under equilibrium
Ar	Transformation temperature upon cooling
BCC	Body Centered Cubic
Bs	Bainite start transformation temperature
Ms	Martensite start transformation temperature
Mf	Martensite finish transformation temperature
SAG-FW	Shielded Active Gas – Forge Welding
CCT	Continuous Cooling Temperature
CE	Carbon Equivalent
FCC	Face centered cubic
HV10	Hardness Vickers 10 kg load
IC	Intercritical
MA	Structure consisting of retained austenite and martensite
Wt%	Weight percent

c	Specific heat capacity
k	Thermal conductivity
q	Heat flux
α	Ferrite
γ	Austenite
δ	Standard deviation
ρ	Mass density

1 Introduction

Risers are pipes transporting oil and gas from the seabed to a production unit. An example of some riser systems is shown in Figure 1-1. The riser systems provided by FMC Technologies consists of several sections of pipes of approximately 30 feet each. Each section is joined to a threaded connection at either side by TIG welding. The sections consist of two steel qualities; the main body is a C90 steel and the threaded component is of F22 quality.

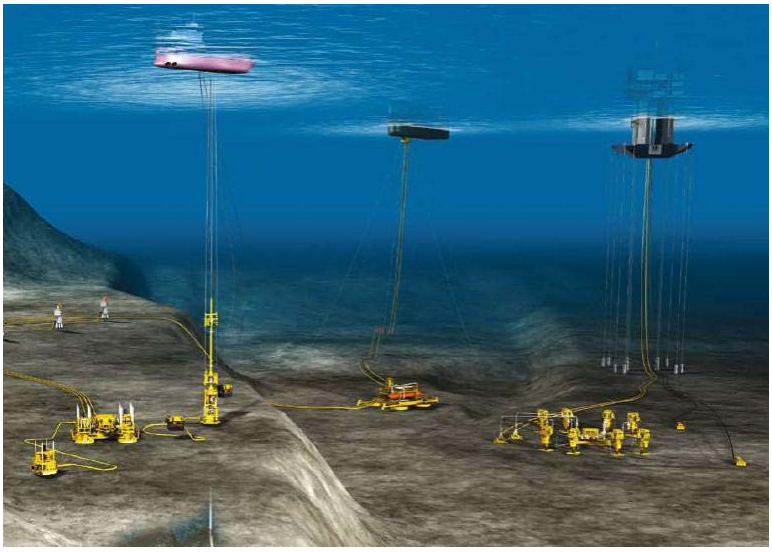

Figure 1-1: Riser systems [1].

This master's thesis was initiated by AMR Engineering in cooperation with FMC Technologies and will explore the possibility of welding the C90 steel by using a Shielded Active Gas Forge Welding (SAG-FW) procedure as an alternative to the conventional TIG welding process. Weld simulations will be conducted on the C90 steel by applying a Smitweld apparatus, which is able to heat the steel piece at high rates by passing a DC current through the specimen. Post weld heat treatment can also be conducted by using Smitweld. The SAG-FW process involves rapid heating of the two joining parts to a selected peak temperature below the melting point, by passing a current through the pipe ends. The mating parts are then forced together by an applied hydraulic pressure, and joined by plastic deformation and diffusion of atoms from both sides. The shielding gas prevents oxide formation in the weld zone. Post weld heat treatment is performed by using an induction coil to control the temperature in the selected area. Desired microstructural features may then be achieved in the heat affected zone.

Solid state welding allows lower peak temperatures than TIG which limits grain growth and does not involve any additives to the materials being joined. Steel qualities which are considered non-weldable from a conventional point of view may yet be fit for solid state welding.

Certification of a welding procedure demands several requirements to be fulfilled. This study will be focusing on satisfying requirements for hardness due to stress corrosion issues as well as achieving acceptable impact toughness properties by applying a proposed welding procedure. Properties of the TIG weld will be discussed and compared with results obtained from weld simulations.

2 Theoretical background

2.1 SAG-FW process

The Shielded Active Gas Forge Welding process is an automatic procedure specialized for joining casings and pipelines for subsea applications. An AC current is applied via several pairs of electrodes attached to the mating joints in order to obtain resistive heating. To avoid oxidation, a purge gas providing a shielding atmosphere is applied in the heat affected area. Cooling may be provided by passing a gas or a fluid internally through the two mating pipes or external flushing of the weld. Some plastic deformation will take place at the weld center upon joining of the pipes. If heat treatment of the weld is necessary, a high frequency induction coil can be placed around the weld to reheat the post quenched structure in order to obtain satisfactory mechanical properties [5].

2.2 Iron-Carbon Metastable equilibrium diagram

The Iron-carbon phase diagram provides invaluable premises for understanding the mechanisms involved in welding processes. Carbon is the most important alloying element and is responsible for many of the properties that can be obtained in steel. Other alloying elements will however, influence the phase compositions and the range of the different phases. Iron is an *allotropic* material meaning it can exhibit two crystal configurations, the *Body Centered Cubic* (BCC) and the *Face Centered Cubic* (FCC) [6] where the FCC structure is the densest configuration of the two. Figure 2-1 shows at which temperature and compositions the different phases exist at equilibrium conditions. It should be clarified that the Iron-Carbon diagram is actually a metastable phase diagram between iron and *cementite* (iron carbide). The stable Fe-C diagram is represented by the dashed lines. Graphite is the true equilibrium phase, but it is hard to obtain for low carbon contents (<1,5 wt% C)[7]. The *alpha* and *delta* phase (α, δ) represents the BCC configuration and the *gamma* phase (γ) the FCC configuration. *α is* referred to as *ferrite, δ as delta-ferrite* and *γ* as

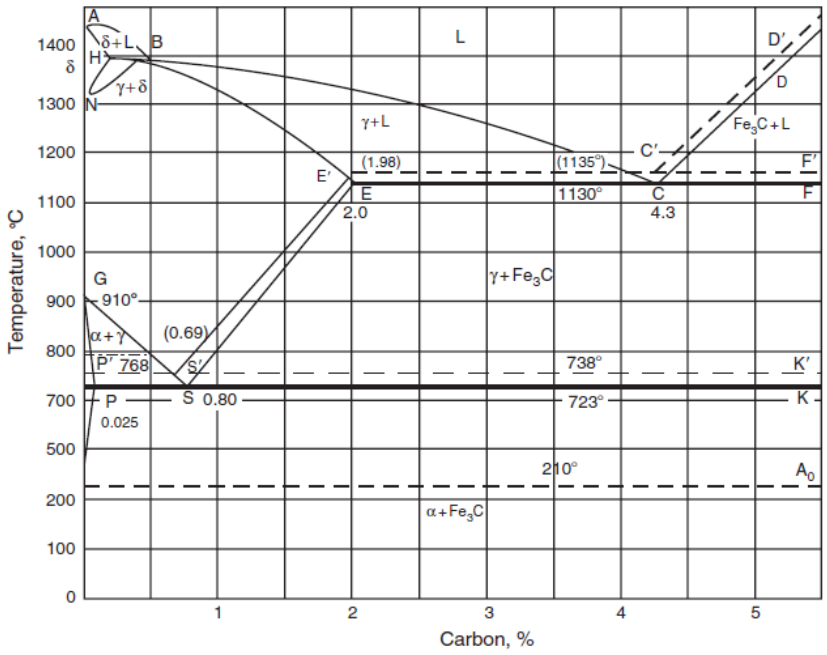

Figure 2-1: Fe-Fe₃C metastable phase diagram [2].

austenite. The steel type used in this study are of *hypo- eutectoid* composition, meaning that its carbon content does not exceed the eutectoid composition of about 0.8 wt% carbon [7]. The eutectoid composition can be found in Figure 2-1 at 723 ˚C at the point marked "S". At lower temperatures ferrite coexists with the intermetallic compound known as *cementite,* Fe_3C. The eutectoid composition of these two phases is referred to as *pearlite* which exhibits a lamellar structure. The temperature at which ferrite and cementite starts to transform to austenite at equilibrium conditions, is referred to as Ae1. The boundary at which ferrite and austenite no longer coexists is referred to as Ae3 and is represented by the G-S line in the phase diagram. To know the whereabouts of these transition boundaries is critical when establishing process parameters during solid state welding and heat treatments and will be described more thoroughly in later sections.

2.3 Metastable phases in steel

2.3.1 Formation of martensite

A steel's hardenability refers to its ability to harden by formation of *martensite* when quenched [6]. In other words, a steel of high hardenability is characterized by high depths of martensitic structure in the post quenched state. Figure 2.2 shows that austenite may dissolve up to 0.8 wt% carbon, which is about forty times more than ferrite which can only dissolve about 0.02 wt%. In both phases the carbon is interstitially positioned within the respective unit cells. When steel is rapidly cooled from a temperature within the austenite region, the transition from austenite to ferrite and cementite is suppressed by the limited diffusion time. The carbon atoms in the austenitic structure are trapped within the FCC structure of the old austenite when trying to transform into ferrite resulting in a non-equilibrium phase. The new structure is a Body Centered Tetragonal (BCT) unit cell where the carbon atoms prevent the cell from obtaining a cubic structure. This structure is called martensite and is a metastable phase, not present in the equilibrium phase diagram. Martensite nucleates at austenite grain boundaries and has a plate or lath shaped morphology.

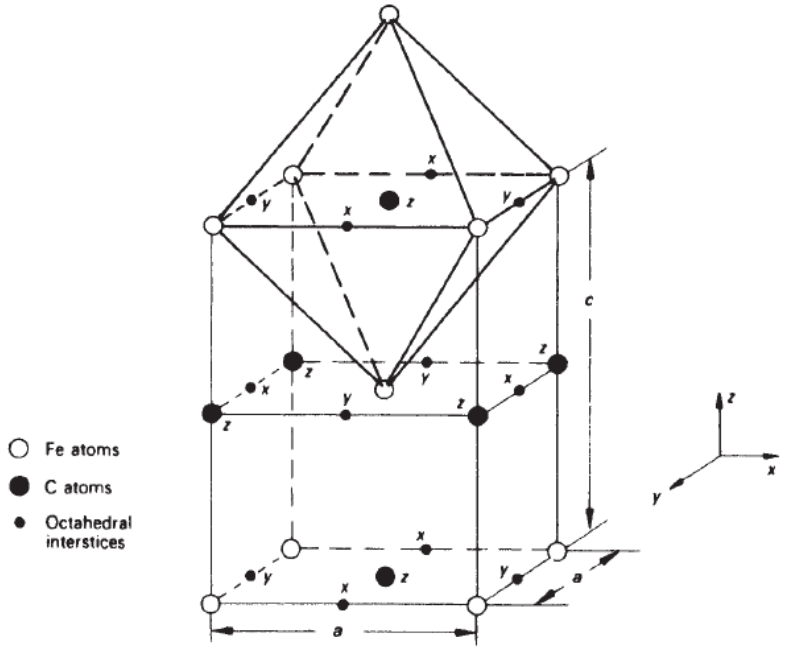

Figure 2-2: Martensite BCT unit cell. The z interstices are fully occupied [7].

Lath martensite is composed of numerous laths configured in a parallel fashion containing a sub structure of high density of tangled dislocations. The parallel laths are of similar size and are often confined, resulting in several packets of laths within a single grain. Plate martensite has a non-parallel morphology and plates may vary considerably in size. Twinning is a regular feature observed in the sub structure of the plate martensite, as well as high density of dislocations. It is suggested that lath martensite has a higher fracture toughness than the plate morphology [8].

The tetragonal distortion of the BCT lattice increases with carbon content, following the equation, [7]:

$$a / c = 1 + 0.045 wt\%C \qquad \textit{Equation 2-1}$$

The austenite transforms to martensite by a displacive process, which can be considered as a shear deformation of the austenite lattice not accompanied by atomic diffusion. The deformation leads to a volume expansion as well as a substantial increase in the dislocation density, especially in steels containing less than 0.5 wt% carbon [9]. The strain and the presence of dislocations associated with the expansion of the lattice also contributes to increased hardening [9]. The laths or plates start to develop at the austenite grain boundaries and pierce through the austenite grain. The interface between the tip of the plates/laths and the austenite is incoherent and allows for fast growth. The plate/lath-austenite interface is composed of the close packed directions of both phases ($<110>_{\gamma}||<111>_{\alpha}$) [10]. The interface is coherent and growth

perpendicular to the plate sides is slow [10]. The martensite morphology may differ depending on the conditions surrounding the transformation. When a shear force is applied to the deforming austenite, a number of dislocation slip systems may activate, reducing the overall strain. The result is a lath like morphology which is common for steels containing less than 0.5 wt% C. Plate martensite develops due to twinning and requires a higher shear force than dislocation glide. This process is more likely to occur in steels of higher carbon content [10].

2.3.2 The kinetics of the martensite transformation

The martensite transformation is considered an athermal process, meaning that the extent of martensite formation depends on the cooling rate below the critical temperature; M_s [9]. The temperature at which martensite starts to develop during cooling depends on the steel composition as well as its initial microstructure. This critical temperature is referred to as M_s and marks the point at which 1 % of the structure is martensitic. When 99 % of the structure is martensitic, the temperature M_f has been reached and the transformation is nearly complete [11]. An empirical equation to predict the M_s temperature has been presented by *Andrews (1965)* and suggests the following relation [12]:

$$M_s(°C) = 539 - 423C - 30.4Mn - 17.7Ni - 12.1Cr - 7.5Mo \qquad \textit{Equation 2-2}$$

In 2002 an improved equation was presented based on a Bayesian neural network model which includes elements such as Silicon, Copper, Cobalt and Wolfram [13]:

$$M_s(°C) = 491.2 - 302.6C - 30.6Mn - 16.6Ni - 8.9Cr + 2.4Mo - 11.3Cu + 8.58Co + 7.4W - 14.5Si \qquad \textit{Equation 2-3}$$

In Figure 2-3 the influence of carbon content is related to the M_s and M_f temperatures graphically.

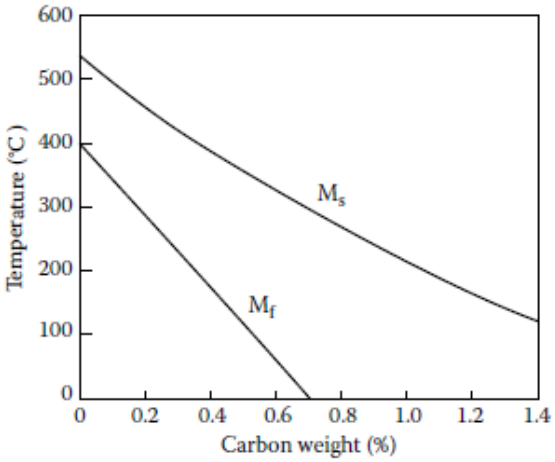

Figure 2-3: M_f and M_s as a function of carbon content [14].

2.3.3 Formation of bainite

For cooling ranges between what is required to obtain martensite and perlite, a structure known as *bainite* may develop. The transformation is an intermediate between martensite and perlite, as it exhibits both diffusive and non-diffusive characteristics. During the transformation ($\gamma \rightarrow \alpha$) the lattice is rearranged; carbon is redistributed and carbides are precipitated. The bainittic structure can be considered a mixture between ferrite and carbides and takes on a lath or plate like morphology [2],[10]. The bainite is classified as either upper or lower bainite, depending on the temperature of the transformation. Lower bainite generally exhibits quite good mechanical properties as opposed to the upper bainite which is hard and brittle [6]. Upper bainite is characterized by the precipitation of Fe_3C carbides in the interface between the bainite laths and may transform at temperatures in the range from 400-500 ˚C [10]. The growth mechanism is similar to that of martensite. In lower bainite, carbides are precipitated within the laths and the carbides are either cementite or ε-carbides. Lower bainite can form at temperatures as low as 250-400 ˚C. Bainite is formed through a shear deformation, not unlike the martensite transformation and will therefore induce a high density of dislocations within the laths/plates [10]. The maximum temperature at which bainite starts to transform may be estimated using the empirical equation [11]:

$$B_s(^\circ C) = 830 - 270C - 90Mn - 37Ni - 70Cr - 83Mo \qquad \textit{Equation 2-4}$$

2.4 Dilatometer curves

Determining at which temperature austenite begins to form upon heating, Ac1, can be performed by measuring the volume change of a given sample during heating. The respective temperature during cooling is referred to as Ar1 and the corresponding equilibrium point as Ae1. If heating and cooling rates are sufficiently low, transformation temperatures can be approximated to be the same as the corresponding equilibrium temperatures. Determining

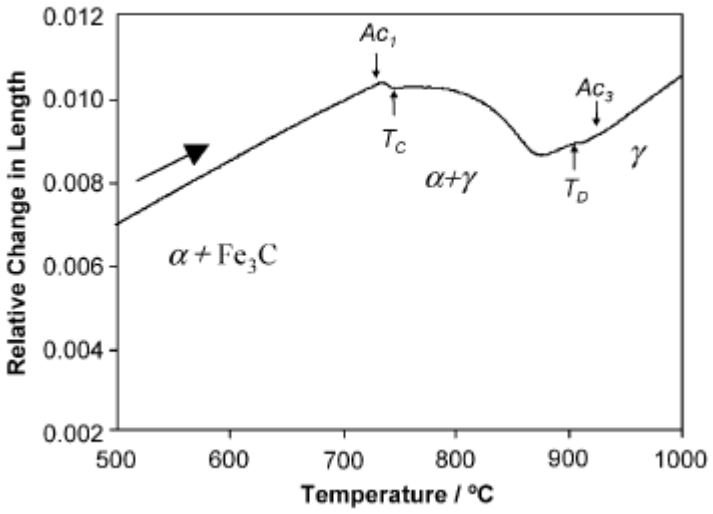

Figure 2-4: $\Delta L/L_0$ of a low carbon steel (0.11 C, 0.5 Mn) upon heating at 0.05 Ks^{-1}[4].

the Ac1 temperature may prove invaluable when considering at which temperature the steel is to be heat treated. There is a volume contraction associated with ferrite being transformed to austenite and this is detected by the dilatometer. Obtaining the equilibrium temperature at which this process occurs may take quite some time due to the slow heating rates required. During heating or cooling at higher rates, the transformation temperature observed will be either higher or lower than Ae1, respectively [4], due to the limited diffusion time. Figure 2-4 shows the specific volume change of iron as a function of temperature ($\Delta l / L_0 = f(T)$). At high cooling rates (quenching) from the γ region, martensite and bainite is expected to be found in the microstructure if carbon is present. These transformations will occur as deviations from the linear thermal contraction observed in the dilatometer curves upon cooling due to their crystallographic nature as can be seen from Figure 2-5.

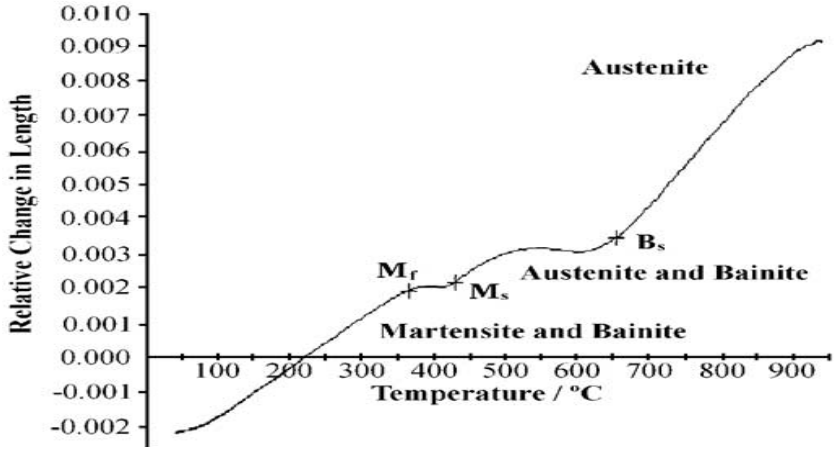

Figure 2-5: Dilatometer curve upon cooling of a low carbon manganese steel (0.07 C, 1.56 Mn, 0.41 Si). Cooling rate: 234 Ks^{-1} [4].

The Ac1 and Ac3 temperatures can be estimated by the empirical equations given by [12]:

$$Ac1 = 723 - 10,7Mn - 16,9Ni + 29,1Si + 16,9Cr \qquad \textit{Equation 2-5}$$

$$Ac3 = 910 - 203\sqrt{C} - 15.2Ni + 44.7Si + 31.5Mo - 11Cr + 700P \qquad \textit{Equation 2-6}$$

The heating rate at which equation 2-5 and 2-6 are based on, have not been addressed in [12].

2.5 CCT diagrams

The iron-carbon phase diagram provides fundamental information of the microstructural behavior at equilibrium conditions. Equilibrium is seldom reached in practice as the system

requires a great deal of time complete its reactions. During cooling at rates substantially higher than what is needed to obtain equilibrium, structures which the phase diagram does not include may appear. Continuous Cooling Transformation (CCT) diagrams provide information about the expected structures achieved during a wide range of cooling rates as well as the amount of the transformation products. By applying such a diagram, temperature and time parameters can be managed to achieve the desired structure. As the amount of alloying elements influences the conditions of nucleation and growth circumstances in different ways, these diagrams may vary for different steel qualities. Austenitizing temperature and grain size of the base structure may also affect the transformation kinetics. The CCT diagram in Figure 2-6 shows an example of how a certain steel quality will react to different cooling rates with the assumption that austenite is the initial structure prior to quenching. The dashed lines represent the thermal path at which the steel is being cooled at. From Figure 2-6 the martensite and bainite phase is expected for high and intermediate cooling rates and these structures are not presented in the equilibrium phase diagram as they are metastable phases.

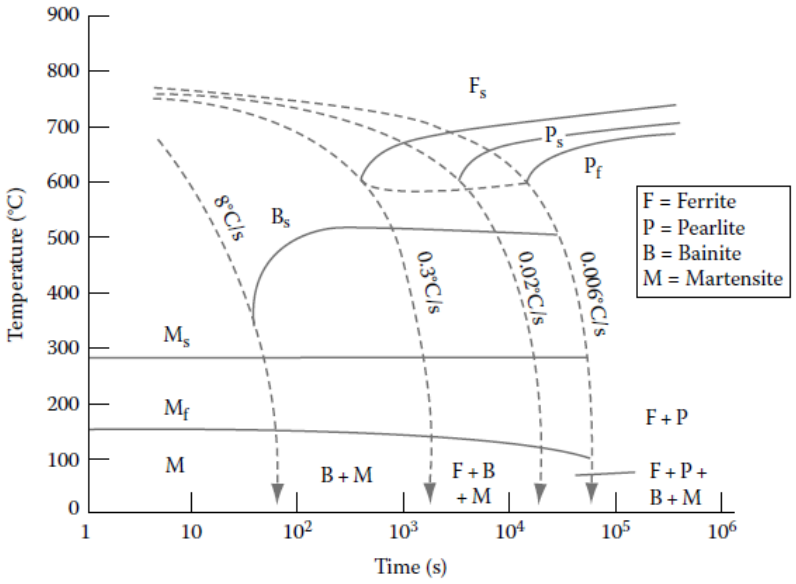

Figure 2-6: CCT curve for SAE 4340 steel [14].

The temperature at which martensite starts to transform can be approximated using Equation 2-3. The highest bainite transformation temperature can also be approximated based on the chemistry (Equation 2-4) but the transformation takes place over a wider temperature interval.

CCT diagrams can be constructed by combining results from dilatometer measurements and microstructural analysis at samples cooled at different rates.

2.6 Quenching and heat treatment

The untempered martensite obtained after quenching is generally very hard and brittle. For most applications a certain degree of ductility is required as well as sufficiently high strength. During tempering, the martensite structure may respond in different manners depending on the choice of tempering temperature and time as can be seen from the example given in Figure 2-7. The tempering process is generally conducted isothermally at a temperature below the austenitizing temperature (Ae1) [14].

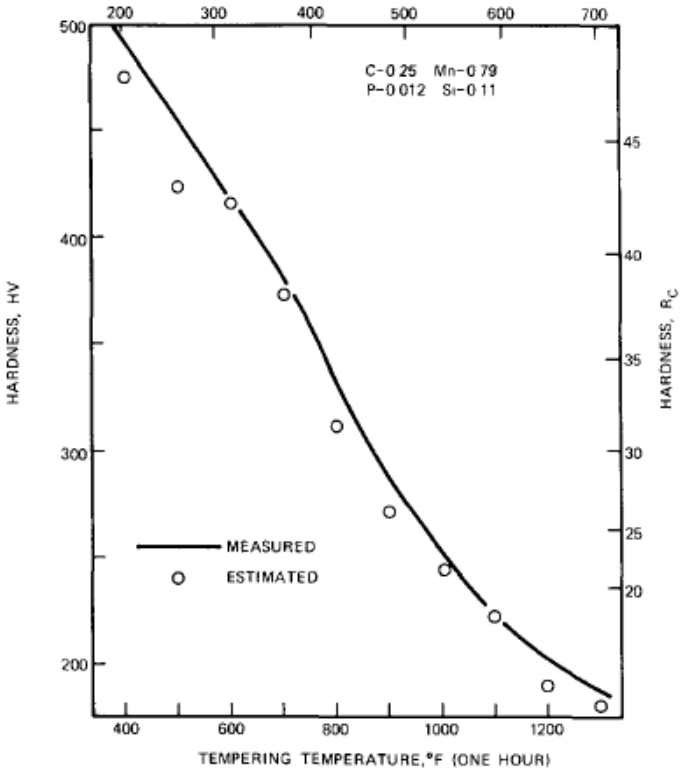

Figure 2-7: Martensite hardness vs. tempering temperature for a 0.25C, 0.79Mn, 0.012P, 0.11Si steel [15].

The first change in the tempering process is segregation of carbon which leads to a decrease in the tetragonality of the martensite unit cell. At low temperatures (<250 ˚C) metastable carbides such as ε-Fe_2C_4 nucleate in the martensite structure resulting in a precipitation hardening of the martensite [14], [7]. At temperatures between 200-350 ˚C retained austenite decomposes to ferrite and acicular cementite forms. At higher temperatures the cementite becomes coarser and grows at the expense of the less stable ε-carbides. Above 350 ˚C the martensittic structure has completely lost its tetragonality [10]. Above 600 ˚C the cementite loses its plate/lath shaped

morphology and becomes spherical [2],[16]. The nucleation sites for the cementite is frequently martensite lath boundaries at lower temperatures [16]. Recovery of the structure generally occurs at temperatures above 400 ˚C. During this process the lath martensite structure, containing both low and high angle grain boundaries, develops into a more fine grained acicular structure by annihilation of low angle dislocation boundaries [16]. The density of Fe_3C particles plays an important role pinning migrating grain boundaries. Above 600 ˚C recrystallization occurs, resulting in ferrite grains developing into an equal axis structure [10]. Alloying elements slows the recrystallization process by the pinning action provided by their respective carbides formed at the grain boundaries. In steels containing sufficient amounts of Mo, V, W and Ti an effect referred to as *secondary hardening* occurs at temperatures above 600 ˚C. The hardening is a result of the carbides formed by these additives. Chromium also forms carbides at these temperatures, but due to the fast coarsening of these particles the hardening effect is small. The chromium does however retards softening [16]. Figure 2-8 shows the stable phases of the ternary composition of Fe-C-Cr-Mo at an isothermal section at 700 ˚C. The steel used in this study (C90) contains 0.25 wt% carbon, and may therefore deviate from the diagram presented here, but its illustrative purpose is still maintained.

At 700 ˚C the carbon binds many alloying elements to form stable carbides. During carbide formation the alloying elements in solid solution is depleted at the expense of carbide growth. Figure 2-9 shows the equilibrium phases at an isothermal section of 1050 ˚C. For compositions of low levels of carbon and chromium, the alloying elements are fully dissolved in the matrix.

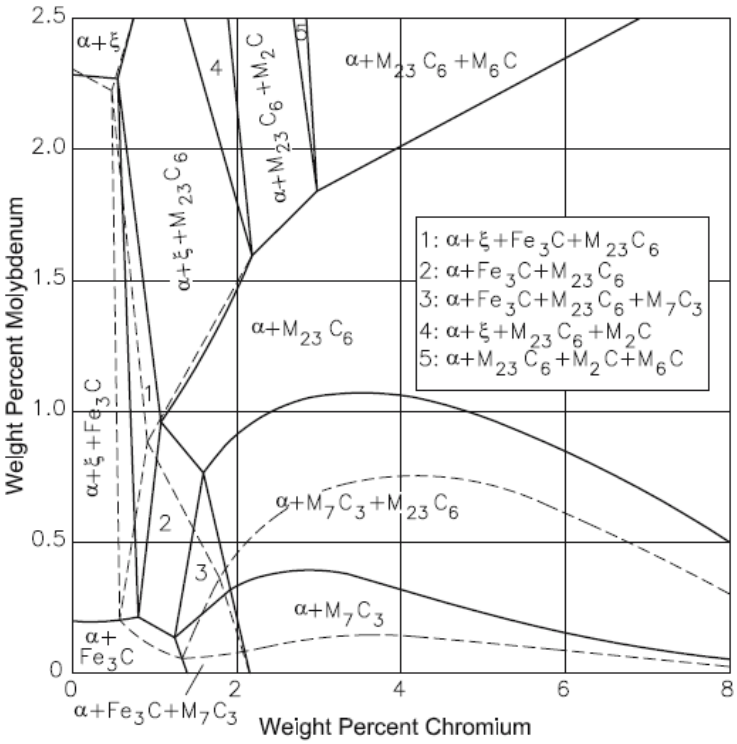

Figure 2-8: C-Cr-Fe-Mo phase diagram. Isothermal section at 700 ˚C and 0.35 wt% carbon [3].

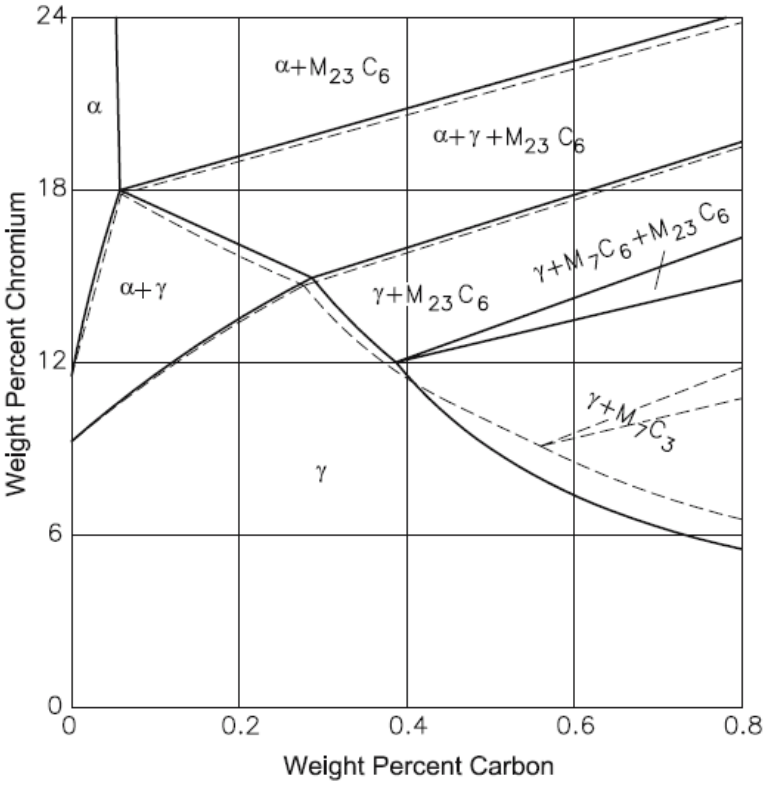

Figure 2-9: C-Cr-Fe-Mo phase diagram. Isothermal section at 1050 ˚C at 1 wt% Mo [3].

2.7 Intercritical zone

The intercritical (IC) zone in the vicinity of the weld center is characterized as hard and brittle. Due to the temperature gradient throughout the welded piece, some areas will experience a non-desired temperature path. The intercritical zone refers to the areas whose peak temperature is between Ac1 and Ac3, i.e. in the two phase range of the phase diagram. In Quench-Tempered (QT) steels, the base structure is tempered martensite. Upon heating, austenite nucleates at the old austenite grain boundaries from which the martensite has nucleated, and its composition will be close to the eutectoid (0.8 % C). When this structure is cooled down, some austenite may transform to brittle martensite. However, due to the high content of carbon in the austenite, the M_s temperature will be substantially lower (ref. Equation 2-3) leading to the possibility of retained austenite being the result as well. The overall structure now consists of a relatively soft martensitic base with a brittle MA structure along the grain boundaries. This MA structure may act as crack initiating sites as well as aiding the crack to propagate along the grain boundaries resulting in intragranular fractures. By tempering this structure at a temperature close to Ac1, carbides may precipitate decreasing the carbon content in both the martensite and the retained austenite which, in turn increases the fracture toughness. After the tempering session is complete, the retained austenite is no longer of eutectoid composition and may easier transform to martensite.

2.8 Weldability/Carbon equivalents

The microstructure in a weld depends much on the composition of the given steel. The carbon content plays a major role in the weld process as it increases the steels hardenability. For conventional welding, steels are considered non-weldable if their *Carbon Equivalent* (CE) exceeds a pre-defined value. The purpose is to convert other non-carbon alloying elements into carbon equivalents as the iron-carbon phase diagram is better understood than multi alloyed systems. The alloying elements are scaled by a coefficient based on their ability to retard the $\gamma \rightarrow \alpha$ transformation. For steels containing more than 0.18 wt% carbon, the expression provided from the International Institute of Welding is commonly used to determine the steel's weldability [7]:

$$CE = C + \frac{Mn + Si}{6} + \frac{Ni + Cu}{15} + \frac{Cr + Mo + V}{5} wt\% \qquad \textit{Equation 2-7}$$

For CEs above 0.4 wt% the steel is not easily welded due to the high ability to form martensite [7]. The C90 steel examined in this study has a CE value of about 0.76 and should, according to Equation 2-7 not be fit for welding.

3 Experimental

3.1 Base material and machining

The C90 steel was provided by FMC Technologies and was delivered as two pipes. In order to perform the welding simulations, the pipes had to be machined into smaller square rectangles of proper dimensions (11x11x100 mm). The machining was performed at the university workshop. A notch indicating the outer edge of the pipe was placed on every sample as can be seen from Figure 3-1. Table 3-1 presents the chemical composition for the C90 quality provided by FMC Technologies. The measuring method at which this composition has been determined, is unknown to the author.

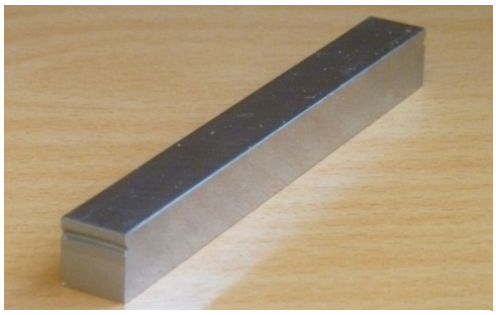

Figure 3-1: As cut sample. Notch indicates outer end of pipe.

Table 3-1: Chemical composition of C90.

Element	C	Mn	Si	P	S	Ni	Cr	Mo	Cu	V	Nb	Al	N	Ti	Sn
wt%	0.25	0.51	0.23	0.009	0.001	0.05	1.07	0.81	0.08	0.004	0.026	0.04	0.048	0.02	0.006

3.2 Dilatometry

A dilatometer experiment was performed on the C90 base material to determine the Ac1 and Ac3 temperatures at low heating rates. The experiment was conducted using a Netzsch DIL 402 C apparatus. The steel sample (5x5x25 mm) was heated at a rate of 150 °C/hour up to 900 °C and held at peak temperature for 60 minutes before it was cooled to room temperature at the same rate. A second cycle was performed to determine whether the transformations would take place at different temperatures if the base structure was closer to its equilibrium state. A protective atmosphere of N_2 gas was used to limit oxidation of the sample during the experiment. The purge gas was added at a rate of 30 ml/min. Figure 3-2 shows the apparatus applied for the experiment. The objective of the experiment was to determine the maximum temperature the steel could be heat treated at without exceeding the Ae1 temperature, as well as mapping the range of the two phase region. The choice of peak temperature was based on the Ac3 value calculated from Equation 2-6.

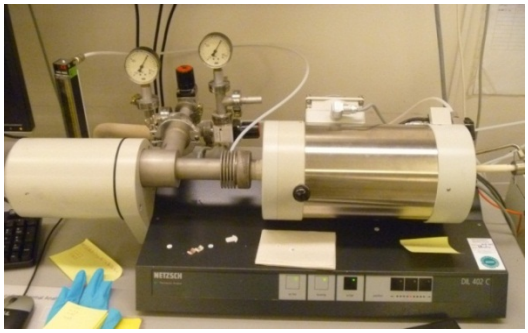

Figure 3-2: The apparatus applied to perform accurate dilatometer experiments.

The Ac3 temperature for the C90 steel is according to calculations 824 ˚C. A peak temperature of 900 ˚C was selected to make sure the sample was clear of the two phase region at Tpeak during the heating cycles. Upon heating at 0.03 ˚C/s it has been assumed that the transformation temperatures observed from the experiment, are approximately the same as the corresponding equilibrium transformation temperatures. From this point on, transformation temperatures obtained from experiments will be presented with its corresponding cooling or heating rate. As an example, $Ac1_{,60}$ refers to the transformation temperature observed upon heating at 60 ˚C/s.

3.3 Welding simulation

The welding simulation was carried out using a SMITWELD-Thermal Cycle Simulator model 1405 apparatus at SINTEF's facilities at NTNU. A K-type thermocouple was spot welded on the outer side of the former pipe at the center of each sample prior to the weld simulations. A dilatometer instrument was applied to determine phase transformations during heating and cooling and the results were logged for each cycle. The selected weld cycles were programmed on the connecting computer with the proper software. Each heat cycle was given a number to correlate the given sample to its thermal history. The heating rate of each cycle was set to 160 ˚C/s and the given cooling rate is applied when the sample temperature is reduced to 920 ˚C after being heated to its peak temperature. Samples, whose peak temperature deviated more than ± 20 ˚C from the pre-selected temperature, were discarded. The Smitweld apparatus heats the steel sample by passing a direct current through it via two clamps at either end, in order to obtain ohmic heating (Joule heating). The clamps are set 10 mm apart defining the heat exposed volume of the specimen. Water cooling (tap water) at approximately 5 ˚C is applied via the clamps. A typical programmed thermal cycle is presented in Figure 3-3. The number of samples subjected to weld simulation and their corresponding thermal path is presented in Table 3-2.

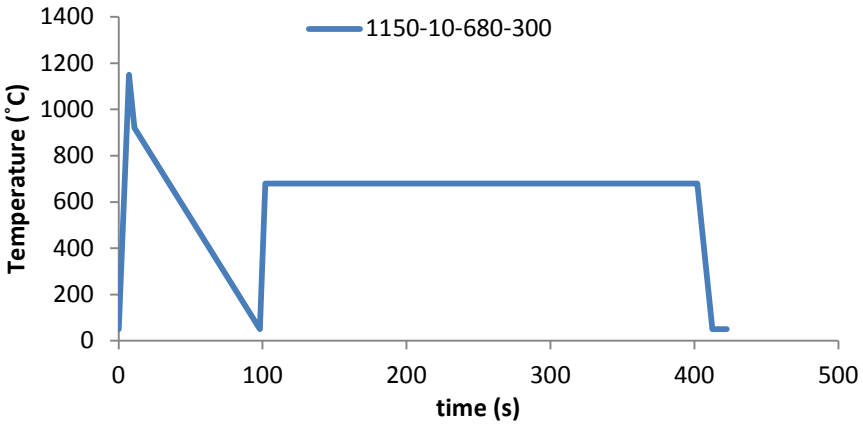

Figure 3-3: Example of preprogrammed thermal cycle of a weld simulated sample.

Table 3-2: Weld simulation and tempering: Numbering of samples and thermal history.

T_{peak} [˚C]	Cooling rate [˚C/s]	Tempering temperature [˚C]	Tempering time [s]	# of parallels	Abbreviation
1150	60	-	-	1	1150-60
1150	10	-	-	1	1150-10
1150	60	680	1/300/1200/3600/10800	4/4/4/1/3	1150-60-680-1/300/1200/3600/10800
1150	10	680	1/300/1200/3600/10800	4/4/4/1/3	1150-10-680-1
1150	60	735	300/1200	4/4	1150-60-735-300/1200
1150	10	735	300/1200	4/4	1150-10-735-300/1200
1150	60	720	300/1200/3600/10800	4/4/1/3	1150-60-720-300/1200/3600/10800
1150	10	720	300/1200/3600/10800	4/4/1/3	1150-10-720-300/1200/3600/10800
800	60	-	-	1	800-60
800	10	-	-	1	800-10
750	60	-	-	1	750-60
750	10	-	-	1	750-10
800	60	680	3600/10800	1/3	800-60-680-3600/10800
800	10	680	3600/10800	1/3	800-10-680-3600/10800
750	60	680	3600/10800	1/3	750-60-680-3600/10800
750	10	680	3600/10800	1/3	750-10-680-3600/10800

3.4 Tempering

Post weld heat treatment was performed in both Smitweld and furnace. Tempering times up to twenty minutes was conducted in the Smitweld apparatus, while longer tempering times was carried out in a Nabertherm C290 air circulating furnace. A thermocouple was spot welded onto the surface of a reference sample that was subsequently placed in the furnace at temperatures of 680 and 720 °C to monitor the heating rate. The reference specimen was placed at the same position in the furnace during both cycles. The temperature was measured with an Amprobe TM45A device. Tempering of the samples later on was performed in the vicinity of the position where the temperature had previously been monitored.

3.5 Charpy V

Impact toughness was tested with a Zwick 450 J apparatus at Sintef's laboratory in Trondheim. The samples were prior to testing cooled to -20 °C in ethanol. Full size Charpy tests were performed and the samples were machined according to ASTM standards for notched bar impact testing of metallic materials [17]. The geometry of the full size Charpy V test bar is presented in Figure 3-4.

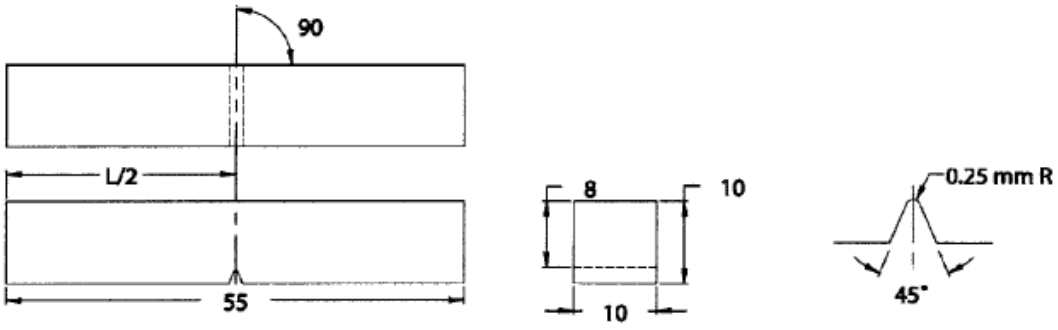

Figure 3-4: Dimensions of the notched bar used for full size Charpy V testing [17]. Lengths in mm.

The notch was placed at the same position as the thermocouples during weld simulation to ensure control of the thermal history in the fractured cross section. Up to three samples from each thermal cycle parallel were tested.

3.6 Microscopy

The weld simulated samples were cut approximately 10 mm from either side of the weld center and molded using a Struers Prestopress – 2 apparatus. Struers RotoPol – 31 was applied for grinding and polishing of the specimens. A 2 % Nital solution (2 % HNO_3, 98 % ethanol) was used to etch the polished surface to expose the steels microstructure.

Microscopy was performed using a Leica MEF4M microscope and a Jenoptic CCD camera aided by the Image Access Easy Lab 7 software.

3.7 Modeling

Comsol, a multi-physics software was used to simulate the temperature distribution along the length axis of the welded specimens. In the model, an arbitrary potential was set over the length of the heated area to obtain sufficiently high temperatures. An inward heat flux was applied on the exposed surfaces, and the surrounding temperature set to 20 ˚C with a heat transfer coefficient set to 5 [W/ (m^2K)]. The water cooling system has been assumed to be sufficient to maintain a constant temperature of 5 ˚C at the respective endpoints. Material constants and properties of an AISI 4340 steel were imported from the software material library and applied to the domain.

3.8 Hardness measurements

Vickers hardness tests (HV10) were conducted in accordance with EN10045/1. The indentations were set 6 mm from either side of the weld center with 1 mm spacing. In addition two indentations were made above and below the weld center. The apparatus used for the hardness measurements was a Struers Duramin – A2500. Prior to hardness testing, the specimen surface was ground down approximately 0.5 mm, to remove oxide layers and to prevent hardness indentations in a surface subjected to decarburization. Figure 3-5 shows a low magnification image of a sample subjected to hardness measurements.

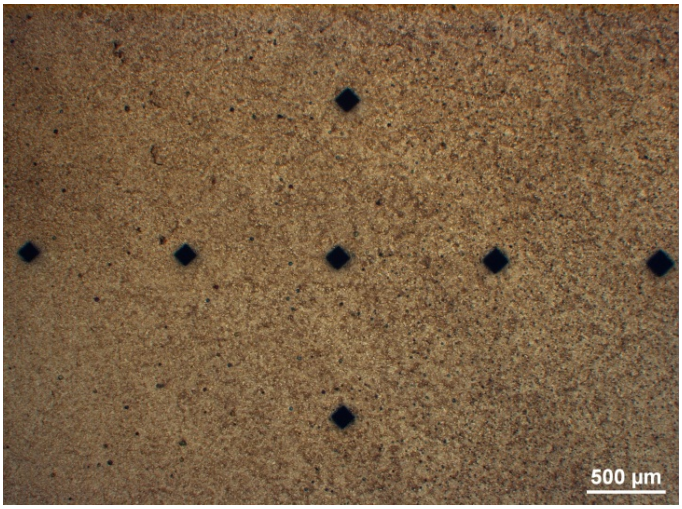

Figure 3-5: Positioning of HV10 indentations in HAZ. Horizontal axis is parallel to length axis of sample.

The intercritical zone of the weld was measured based on a model approach, described in section 4.4.3. Temperature data was collected for each length unit along the weld simulated specimen

generated by the model. The Ac1 and Ac3 temperatures found for the given heating rates, was used to determine which intercritical temperature to select. An intermediate temperature between Ac1 and Ac3 was selected and the corresponding position of the welded specimen was then subjected to hardness testing.

3.9 Fracture surface

A Zeiss Ultra 55 Limited edition Scanning Electron Microscope (SEM) was applied to investigate the fracture surface of the Charpy V tested samples. The SmartSEM Ultra55 software was used in connection with the apparatus. The images obtained were taken with an accelerating voltage of 15 kV and magnification varying from 10-500X. A Secondary Electron Imaging (SEI) detector was applied to obtain the images.

A Wild Heerbrugg Photomakroskop M400 and a connecting Leica DC 300 CCD camera were applied to determine macrostructure of the fractured cross section.

4 Results

The result section will cover much of the experimental data extracted from the experiments. This involves welding/tempering cycles, hardness measurements, impact toughness, dilatometer curves and macro/microstructure images. Supplementary data can be found in the appendices.

4.1 Properties of the C90 steel

The C90 steel is a Quenched Tempered steel with a base structure consisting of tempered martensite and provides the basis for all experiments conducted in this work. In Table 4-1 some physical properties of the C90 steel is presented, and includes calculated values as well as data extracted from experiments.

Table 4-1: Some physical properties of the C90 steel.

	Calculated	Experimental
Ac1/Ac1$_{0.03}$	741.5 ˚C	743 ˚C
Ac3/Ac3$_{0.03}$	845 ˚C	812 ˚C
M_s	387.3 ˚C	369 ˚C
B_s	572.6 ˚C	-
Carbon equivalent (CE)	0.76	
Vickers Hardness (HV10)	-	236 ± 1

The experimental values found for Ac1$_{0.03}$ and Ac3$_{0.03}$ are based on dilatometer results which are presented in chapter 4.2. Figure 4-1 shows the tempered martensitic microstructure of the C90 material as delivered from FMC Technologies.

Figure 4-1: Microstructure of C90 prior to weld simulation.

4.2 Ac1 and Ac3 temperatures

The observed transformation temperatures tend to increase at high heating rates due to the limited diffusion time. For the dilatometer experiment a low heating and cooling rate of 2 ˚C/min was selected to determine the transformation temperatures under more conservative conditions than those expected during the welding simulations.

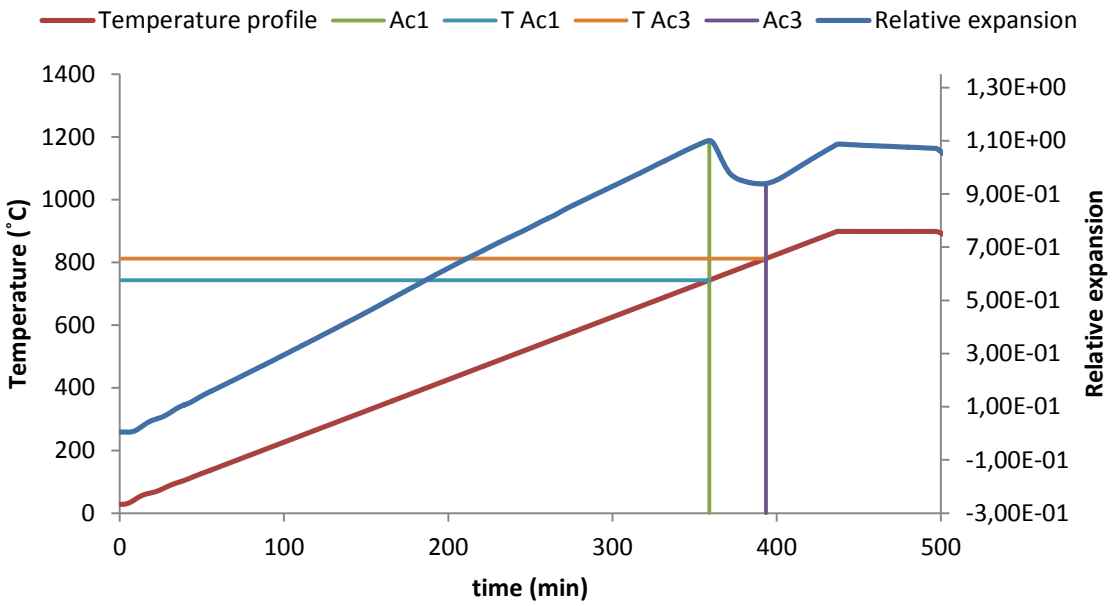

Figure 4-2: Dilatometer results.

The $Ac1_{,0.03}$ and $Ac3_{,0.03}$ temperatures were observed at 743 ˚C and 811 ˚C respectively and can be seen from Figure 4-2. The obtained $Ac1_{,0.03}$ temperature corresponded well with the calculated value from Equation 2-5 which suggested an Ac1 temperature of 741.5 ˚C. The Ac3 temperature was calculated to be 845 ˚C compared to 811 ˚C observed from the dilatometer experiment upon heating at 0.03 ˚C/s. The second heating cycle showed small deviations from the results obtained during the first cycle and the respective transformation temperatures were observed at 745 ˚C and 811 ˚C. The transformation temperatures were determined by subtracting the value at n(t+2dt) with the value at n(t) from the dilatometer data sets. For values lower or equal to zero the derivative is negative, implying the transformation is in progress.

4.3 Temperature profiles during heating

4.3.1 Smitweld

The tempering temperatures applied on the welds were selected to be quite close up to the $Ac1_{,0.03}$ temperature of the material. A 3D model of the temperature profile through the specimen during Smitweld simulation was carried out using the multi-physics software Comsol, in order to design tempering experiments with the highest possible temperature below Ac1. The placing of the sample with the K-element in the weld simulating apparatus is all done by eye and may therefore deviate slightly from being exactly centered. The profiles seen in Figure 4-3 have been calculated at t=0 s to t=4.5 s with dt=0.5 s and are measured along a line over the length surface of the steel bar upon heating to 720 ˚C.

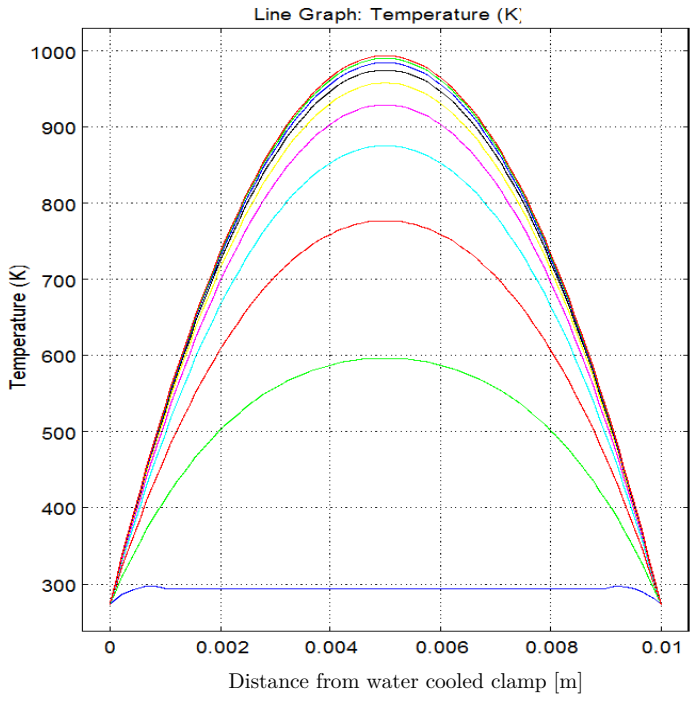

Figure 4-3: Temperature profiles during heating. Tpeak = 720 ˚C.

The profile representing the time at Tpeak was plotted in Microsoft Excel 2011 and added a polynomial regression curve, producing the equation:

$$y(x) = -3 * 10^7 x^2 + 287939x \, [^\circ \mathrm{C}] \qquad \textit{Equation 4-1}$$

The temperature profiles indicate that the highest temperature achieved in the material is not necessary at the position where the thermocouple is placed, if it is not properly centered. According the Equation 4-1 a thermocouple offset $\pm$ 1 mm from the center results in a temperature difference of 18 ˚C. At higher offsets the difference increases rapidly. Figure 4-4 shows the profiles during heating to 1158 ˚C with with dt=1 s and t(Tpeak)=7 s. Figure 4-4 is included to estimate at which sections of the specimen one would expect to find the intercritical zone and has been applied in Section 4.4.4. Figure 4-4 shows a 3D model of the heated sample with temperatures indicated using a color scale.

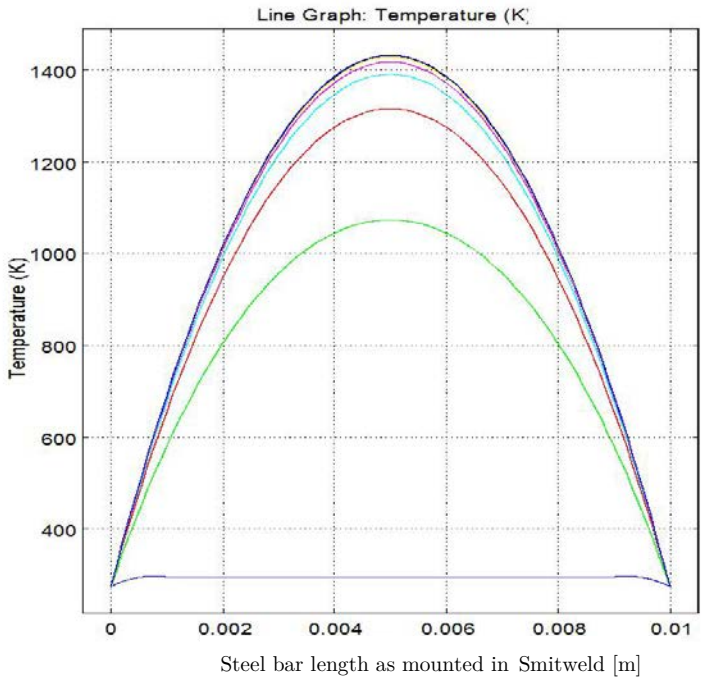

Figure 4-4: Temperature profiles during heating to Tpeak=1158 ˚C.

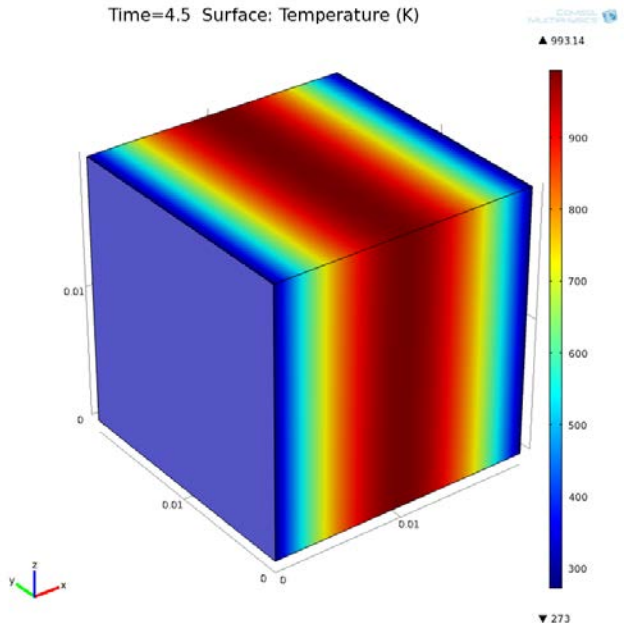

Figure 4-5: 3D temperature distribution of weld simulated area at t=t(Tpeak).

An analytical approach applying the *heat equation over* the length of a heated sample was carried out to compare with the model generated in Comsol. The *heat equation* is presented in Equation 4-2:

$$\rho c \frac{\partial T}{\partial t} = k \frac{\partial^2 T}{\partial x^2} + q(x) \qquad \textit{Equation 4-2}$$

Symmetry was assumed around the sample center (x=0), i.e. T(-L)=T(L)=T_L. The total length of the sample is equal to 2L. The constants ρ, c and k are assumed to be constant with respect to temperature which is also assumed for the generated heat ($q(x) = q_0$). The equation is then simplified to:

$$k \frac{\partial^2 T}{\partial x^2} + q_0 = 0 \qquad \textit{Equation 4-3}$$

When solving for the given boundary conditions in one dimensional space, the solution becomes:

$$T(x) = T_L + \frac{q_0}{2k}(L^2 - x^2) \qquad \textit{Equation 4-4}$$

The solution to the differential equation is a polynomial and exhibits the same features as the temperature profiles obtained by the Comsol software. A plot made with an arbitrary y-axis is presented in Figure 4-6.

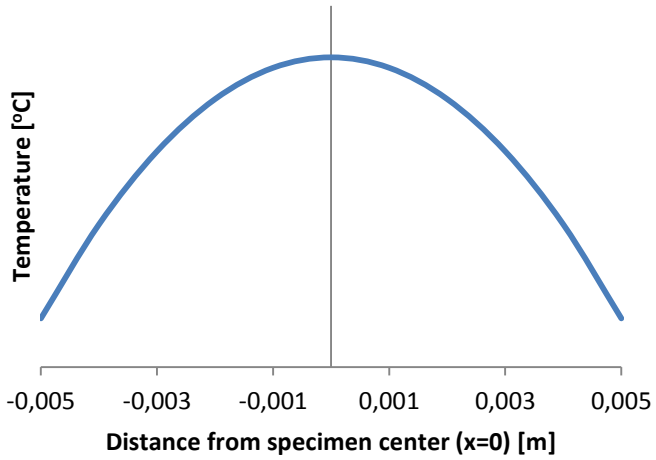

Figure 4-6: Solution to analytical temperature profile during weld simulation. Arbitrary values on y-axis.

4.3.2 Furnace heating

The temperature profile at the surface of a reference sample was measured for samples tempered in the furnace. After 16 and 22 minutes the samples reached their respective peak temperatures at 680 ˚C and 720 ˚C and can be seen from Figure 4-7.

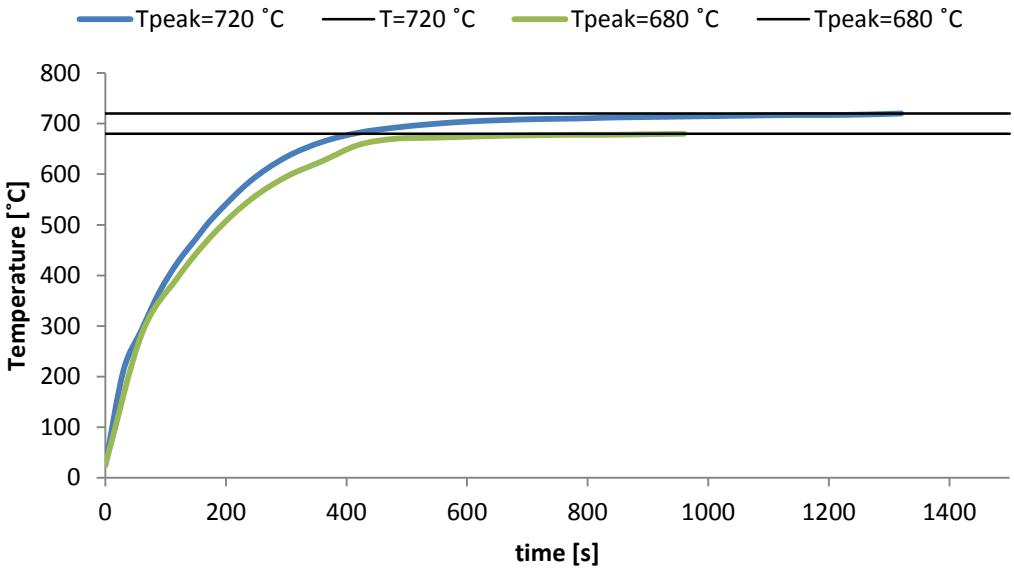

Figure 4-7: Surface temperature profiles of samples tempered in furnace.

4.4 Hardness profiles

4.4.1 Weld center

This section presents hardness values at the weld center of the weld simulated specimens. Vickers hardness (HV10) values have been measured in the heat affected zone of the samples exposed to the different thermal cycles. The indentations have been made in the same isothermal plane as the thermocouple was placed during weld simulation to correlate the thermal history to the microstructure and its properties. Figure 4-8 graphically represents the hardness values obtained for all samples subjected to weld simulation and different tempering times and temperature. The markers in each scatter diagram represent the hardness value found at that given point. Lines are drawn between hardness values for every heat cycle with time being the variable (x-axis). The exact hardness values can be seen in Table 4-2. The tempering temperatures and cooling rates are described by the indicators which are explained in Section 3.3. Note that Figure 4-8 includes measurements from both Smitweld tempering and furnace tempering. Figure 4-9 and Figure 4-10 distinguishes between the two different tempering methods, each representing tempering performed by one of the two methods. Tempering times greater than 1200 seconds was performed in a furnace while shorter tempering times (≤ 1200 s) were carried out by using the Smitweld apparatus.

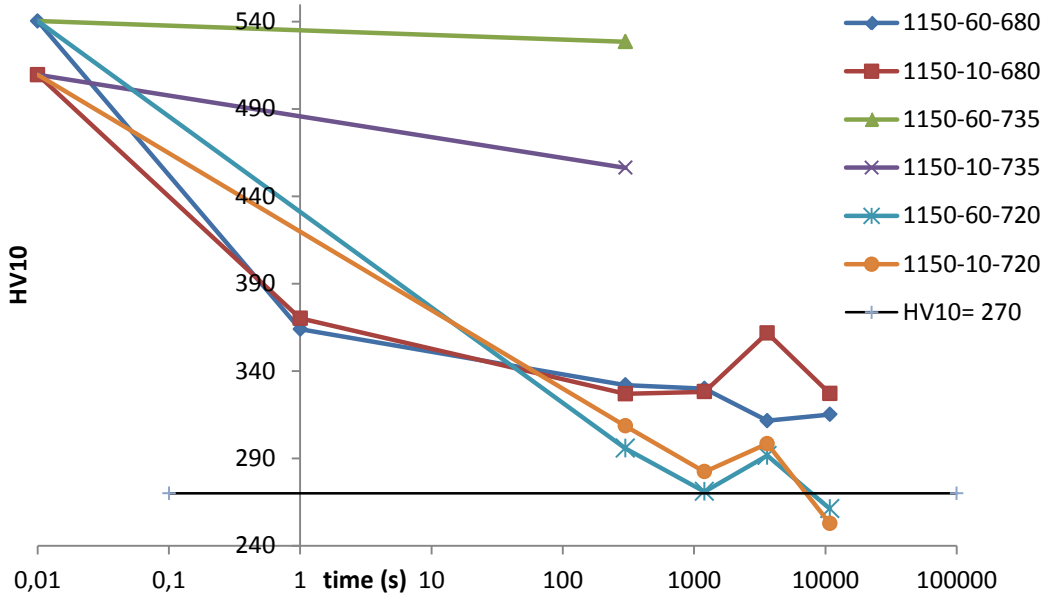

Figure 4-8: Hardness evolution of weld simulated specimens subjected to tempering (0, 1, 300, 1200, 3600, 10800 s).

Significant weld softening is seen for all cycles except the ones tempered at 735 ˚C. The hardness values for these cycles suggest that Ac1 have been exceeded, resulting in martensite formation upon cooling. This will be further commented in Section 4.6.1.

Table 4-2: HV10 values and standard deviation of post weld heat treated samples.

	Smitweld tempering				Furnace tempering	
Thermal history	**0 s**	**1 s**	**300 s**	**1200 s**	**3600 s**	**10800 s**
1150-60-720	540 ± 5	-	296 ± 5	271 ± 2	292 ± 1	261 ± 4
1150-10-720	510 ± 7	-	309 ± 3	282 ± 0	298 ± 9	253 ± 6
1150-60-680	540 ± 5	364 ± 3	332 ± 5	330 ± 4	312 ± 12	315 ± 4
1150-10-680	510 ± 7	370 ± 3	327 ± 5	328 ± 3	362 ± 8	327 ± 3
1150-60-735	540 ± 5	-	529 ± 5	-	-	-
1150-10-735	510 ± 7	-	456 ± 5	-	-	-

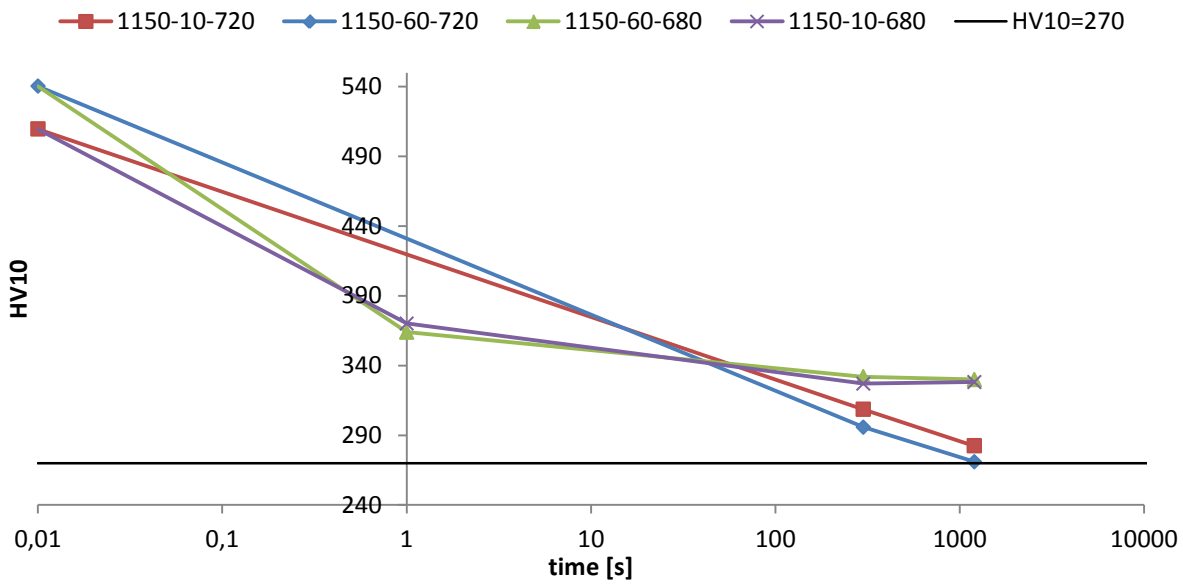

Figure 4-9: Hardness evolution of welded samples subjected to Smitweld tempering.

The parallels subjected to Smitweld tempering shows a clear softening trend with respect to time (Figure 4-9). Tempering at 720 ˚C softens the material more efficiently than what is observed for the 680 ˚C parallel and hardness requirements is nearly obtained after 1200 seconds. From Figure 4-8 a hardness increase is observed for three of the four cycles after tempering at longer durations than 1200 seconds. One and three hour tempering times have been performed in an air circulating furnace and the results are therefore presented separately in Figure 4-10. After three hours, the 720 ˚C parallels were within hardness requirements. The 680 ˚C parallel shows a slight increase in hardness for the longest tempering duration compared to after one hour. A proposed explanation of the different softening paths observed for the two tempering methods will be discussed and presented in Chapter 5.

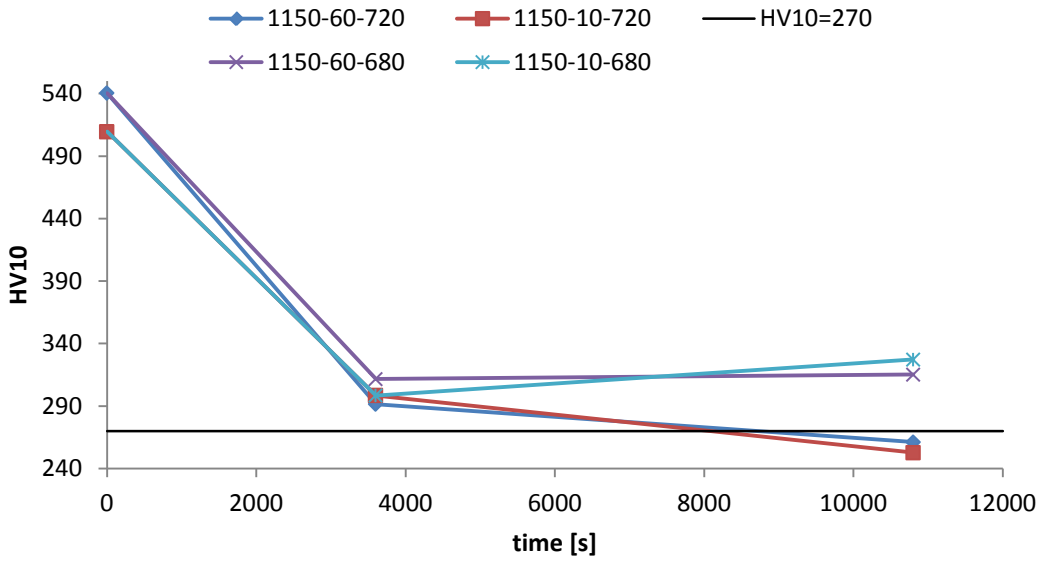

Figure 4-10: Hardness evolution of welded samples subjected to furnace tempering (0, 3600, 10800 s).

4.4.2 HAZ hardness profiles

In this section, hardness profiles of the heat affected zone will be presented for some selected weld cycles of high softening response to post weld heat treatment and can be seen in Figure 4-11 and Figure 4-12. In Figure 4-13 the hardness profile of the as quenched microstructure is presented.

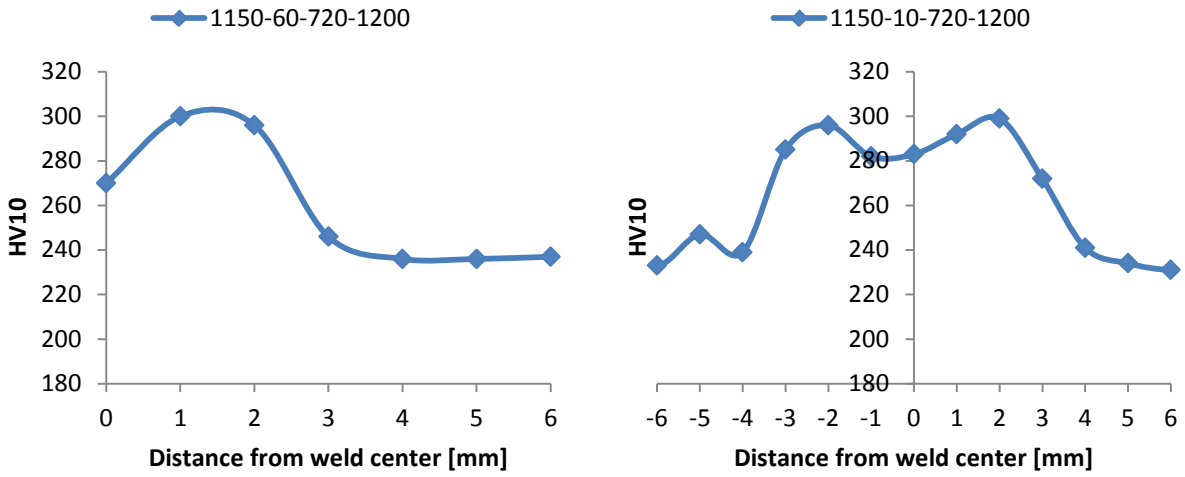

Figure 4-11: HAZ hardness profiles: Left: 1150-60-720-1200 Right: 1150-10-720-1200

The hardness profiles presented in Figure 4-11 shows that the hardest point on the sample is about two mm to either side of the weld center. Upon tempering in Smitweld a rather large temperature gradient is expected over the sample length, as explained in Section 4.3.1. This implies that the structure some distance away from the weld center will be tempered at a lower temperature, resulting in a reduced softening effect. After three hours of furnace tempering, the hardest section is found at the weld center, as can be seen from Figure 4-12.

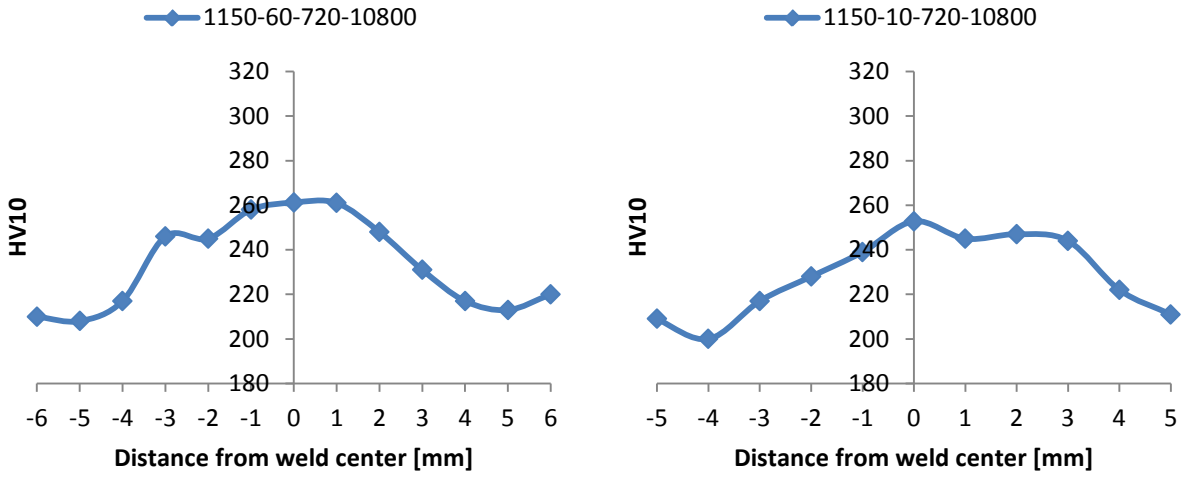

Figure 4-12: HAZ hardness profiles: Left: 1150-60-720-10800 Right: 1150-10-720-10800

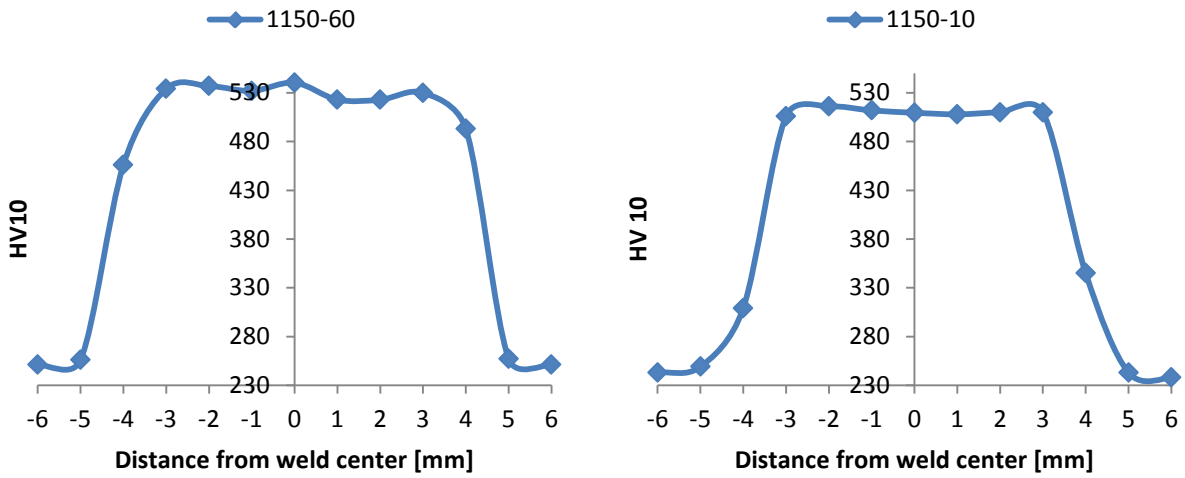

Figure 4-13: HAZ hardness profiles: Left: 1150-60 Right: 1150-10

The hardness profiles obtained after quenching shows a stable high hardness value within three millimeters of the weld sample which is seen from Figure 4-13.

4.4.3 Intercritical zone – initial tests

This section presents experimental results of samples heated to temperatures between the $Ac1_{,0.03}$ and $Ac3_{,0.03}$ obtained from the dilatometer test from Figure 4-2.

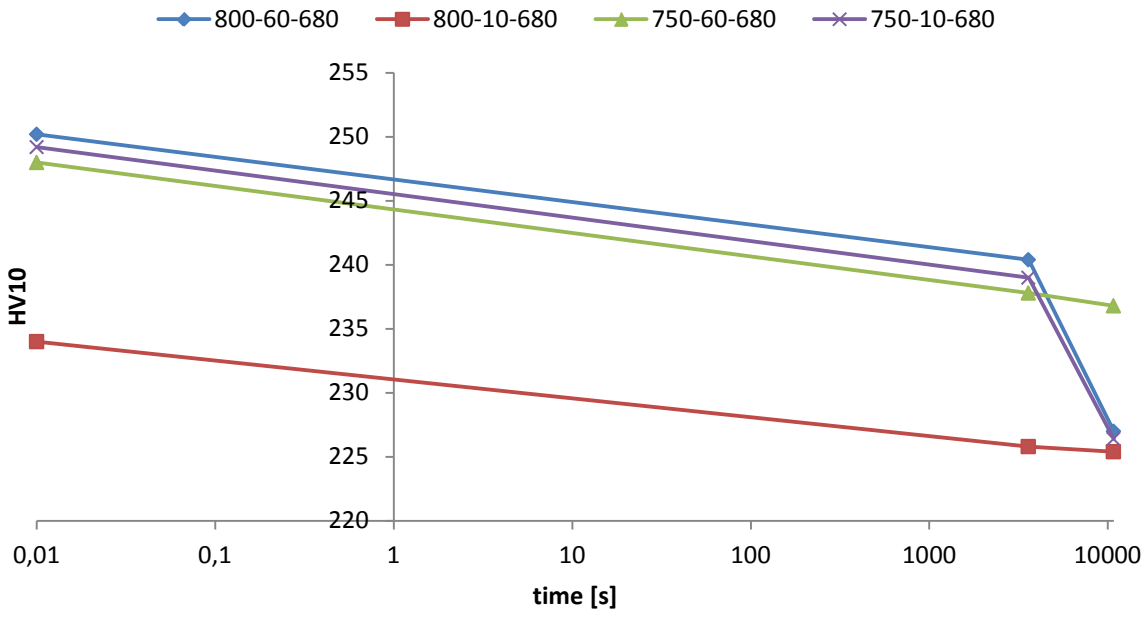

Figure 4-14: Hardness evolution of inter critical zone subjected to tempering in furnace.

The hardness results seen in Figure 4-14 shows that three out of four parallels exhibits a hardness value in the vicinity of those found for the base material (239 HV10) prior to weld simulations. This suggests that only small amounts of martensite were formed upon cooling after being heated to their respective temperatures. The 800-10-680 cycle shows a lower than base material hardness in the as quenched state (t=0) and implies that no martensite was formed during cooling. Upon further heat treatment the material softens slightly, reaching values of 225 HV10 after three hours of tempering at 680 ˚C which can be seen from Table 4-3. The intercritical study performed with the selected peak temperatures (750 and 800 ˚C); have been considered not to be representative for the real intercritical zone obtained during weld simulations since the steel did not enter the two phase region upon heating. Hardness values similar to those observed some 2-3 mm from the weld center in Figure 4-13 was expected for the post quenched structure.

Table 4-3: HV10 values and standard deviation for the intercritical zone subjected to tempering.

Thermal history	0 s	3600 s	10800 s
800-60-680	250 ± 8	240 ± 12	227 ± 4
800-10-680	234 ± 2	226 ± 4	225 ± 5
750-60-680	248 ± 28	238 ± 4	237 ± 2
750-10-680	249 ± 2	239 ± 4	226 ± 5

4.4.4 Inter Critical zone – model approach

The experimental results presented in the previous section have been conducted on structures not subjected to sufficiently high temperatures to reach far enough into the two phase region, for the given heating rates and set temperatures. An approach based on results from the model in Figure 4-3 will be carried out and presented here. From Figure 4-15 it is shown that the two-phase transformation temperatures is found at 801 and 875 ˚C for a heating rate of 60 ˚C/s.

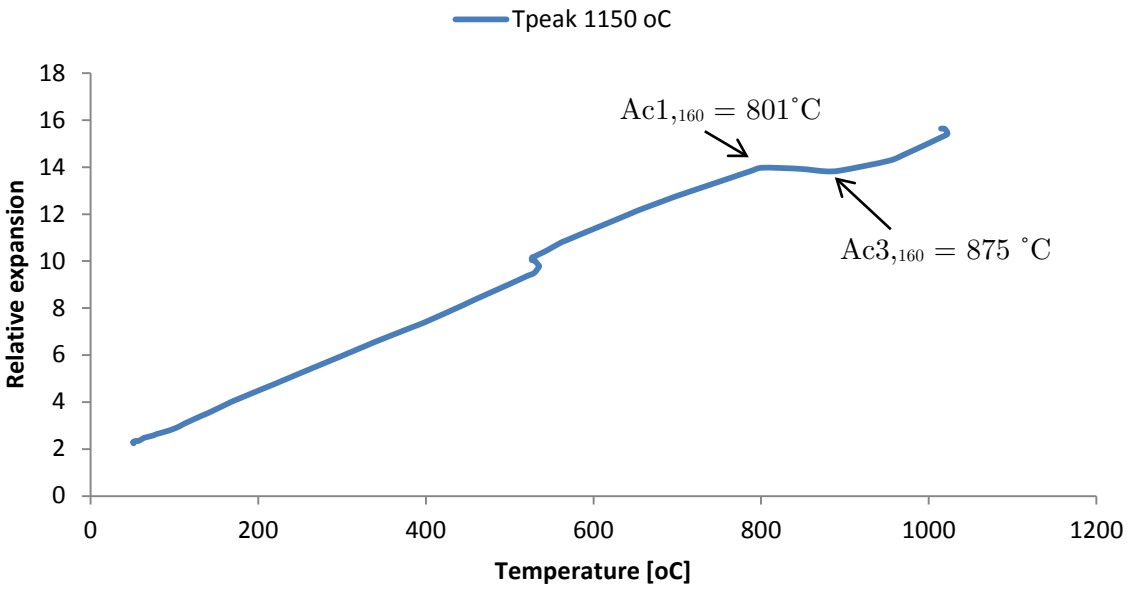

Figure 4-15: Dilation curve upon heating to 1150 ˚C.

Data obtained from the model presented in Figure 4-4 shows that the temperature at 2.7 mm from the weld center is 829 ˚C which according to Figure 4-15, is within the two phase region, and it is at this point the indentations have been made. Only samples subjected to furnace tempering are presented here, because of the uniform temperature distribution obtained by this method.

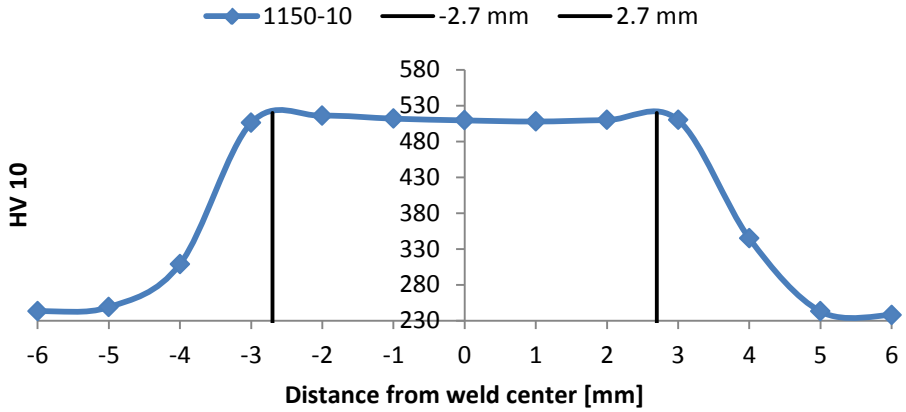

Figure 4-16: Hardness profile in HAZ: 1150-10

Figure 4-16 represents a typical hardness profile observed in the heat affected zone after quenching. The positions where the hardness measurements from the intercritical study have been performed are indicated by the vertical lines at ± 2.7 mm.

The initial values in Figure 4-17 (t=0) are based on the average of the hardness results found 2 and 3 mm from the weld center of the samples. After one hour of tempering at 720 ˚C the IC is considerably softened and hardness requirements are met after three hours.

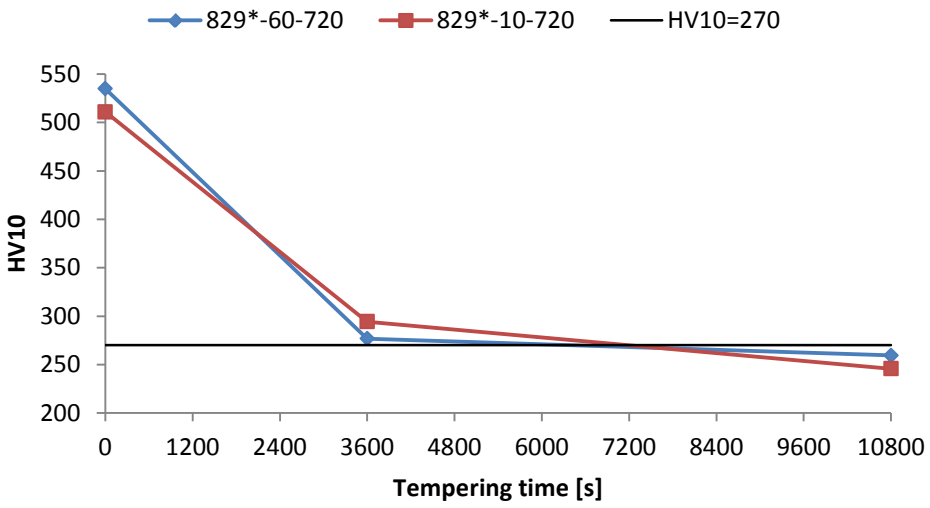

Figure 4-17: Inter critical zone hardness after tempering at 720 ˚C for 0, 3600 and 10800 s.

The peak temperature indicated with *, refers to the temperature found from Figure 4-4 at 2.7 mm from weld center. Table 4-4 shows the Vickers hardness values of the plots made in Figure 4-17.

Table 4-4: HV10 results and standard deviation of the IC zone– model approach.

Thermal history	0 s	3600 s	10800 s
829*-60-720	535 ± -	277 ± 7	260 ± 7
829*-10-720	511 ± -	294 ± 7	246 ± 20

4.4.5 Base material

The base material was tempered at three different durations to determine the softening effect at 720 ˚C. The results are presented in Figure 4-18.

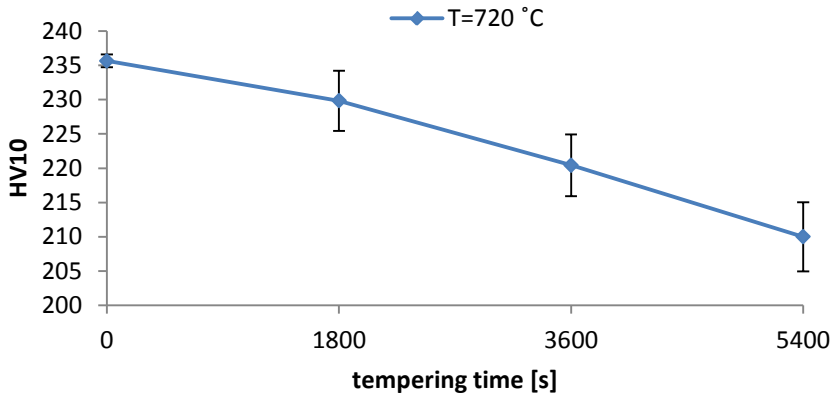

Figure 4-18: Hardness evolution of base material subjected to furnace tempering.

The graph in Figure 4-18 shows a close to linear decrease in hardness during the first 5400 seconds of tempering. This figure has been included to determine the softening expected in the interface between HAZ and base material upon heat treatment.

4.5 Impact toughness

This section presents the impact toughness of the weld center of a selected range of thermal histories. For a more detailed overview of the Charpy test results, see Appendix B: Complete Charpy V chart.

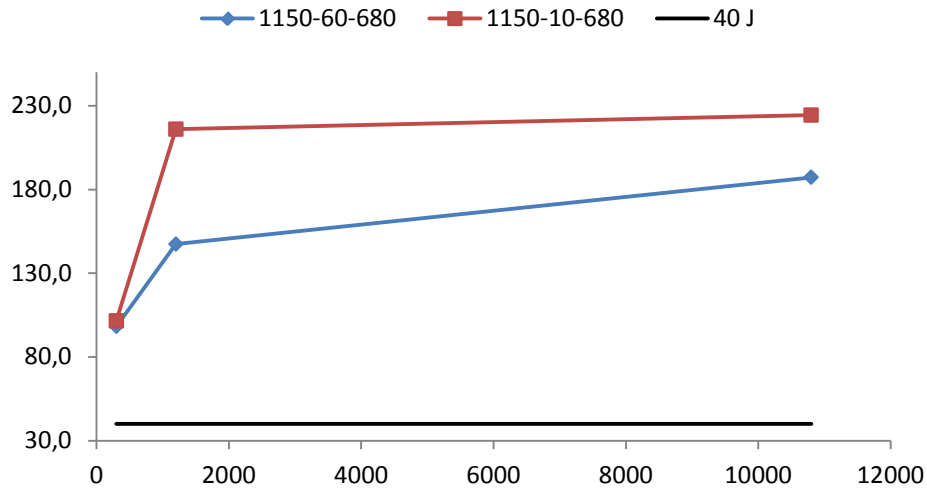

Figure 4-19: Impact toughness vs. tempering time at 680 ˚C.

The impact toughness of the samples tempered at 680 ˚C is rapidly increased during the first twenty minutes of tempering and continues to increase, however not as rapidly, until three hours is reached. Impact toughness is generally higher for samples quenched at 10 ˚C/s.

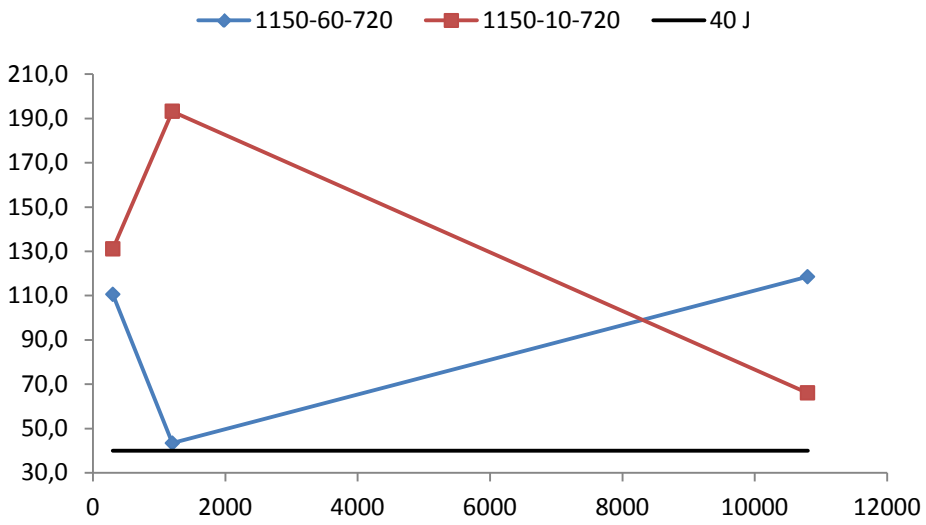

Figure 4-20: Impact toughness vs. tempering time at 720 ˚C.

Tempering at 720 ˚C does not show a clear trend of the tempering effect on the impact toughness. Some high standard deviation values observed in Table 4-5 imply some tempering in the two phase region may have occurred.

Table 4-5: Charpy V results of selected samples.

Thermal history	Kv450 av. [J]	σ	Parallels
1150 - 60 - 735 - 300	34	9	3
1150 - 10 - 735 - 300	43	31	3
1150 - 60 - 680 - 300	98	18	3
1150 - 10 - 680 -300	102	15	3
1150 - 60 - 680 - 1200	147	1	2
1150 - 10 - 680 - 1200	216	15	2
1150 - 60 - 680 - 10800	187	5	2
1150 - 10 – 680 -10800	224	4	2
1150 - 60 - 720 - 300	111	30	3
1150 - 10 - 720 - 300	131	30	3
1150 - 60 - 720 - 1200	43	4	3
1150 - 10 - 720 - 1200	193	2	2
1150 - 60 - 720 - 10800	119	59	2
1150 - 10 - 720 - 10800	66	14	2

4.6 Microstructure

Micrographs of the HAZ were taken in the vicinity of the HV10 indentations to identify the hardness values corresponding to the respective microstructures. Cooling rates after weld cycles followed by tempering does not have a large influence on the HV10 results. Some selected samples representing both cooling rates will be presented here as well as some dilatometer curves to support observations. For a full overview of the dilatometer curves obtained during this work, see Appendix A: Dilatometer plots from Smitweld.

4.6.1 Microstructure of weld center

The microstructure after quenching consists of coarse lath martensite which is shown in Figure 4-21 and several similar sized packets of confined laths can be observed. The outline of the old austenite grains are hard to detect from this structure.

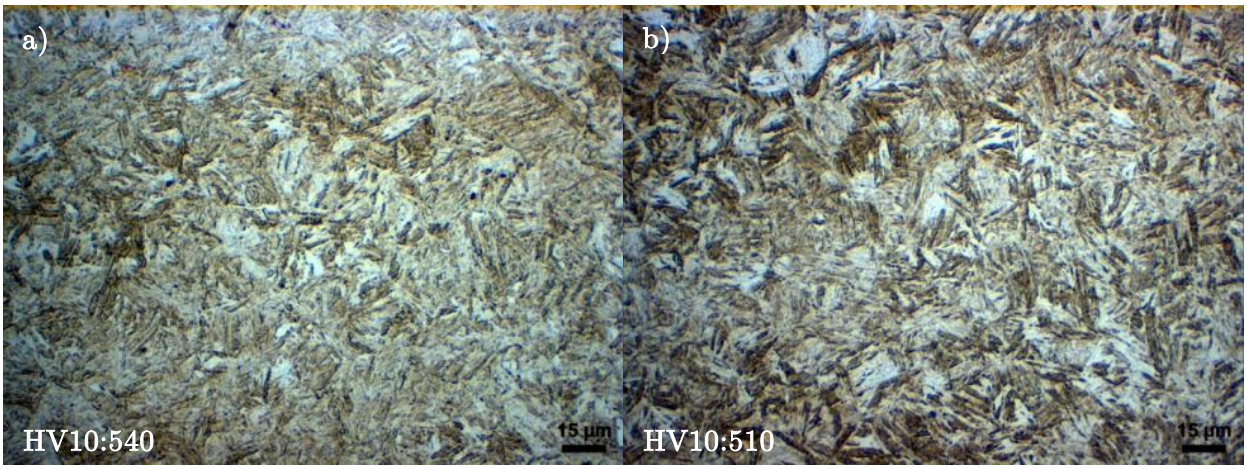

Figure 4-21: Post quenched microstructure: a) 1150-60 b) 1150-10

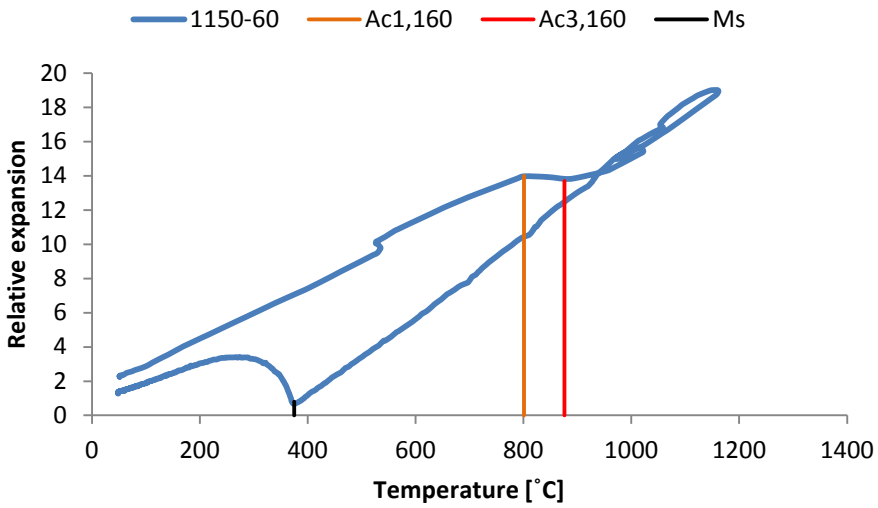

Figure 4-22: Dilatometer curve of sample quenched at 60 ˚C/s.

The dilatometer curve during heating and cooling at the given rates, as presented in Figure 4-22 shows that the structure does not transform to austenite before reaching the $Ac1_{,160}$ temperature at 801 ˚C. $Ac3_{,60}$ is found at 876 ˚C . Upon cooling at 60 ˚C/s, martensite starts to transform at 375 ◦C (M_s). No bainite transformation is observed.

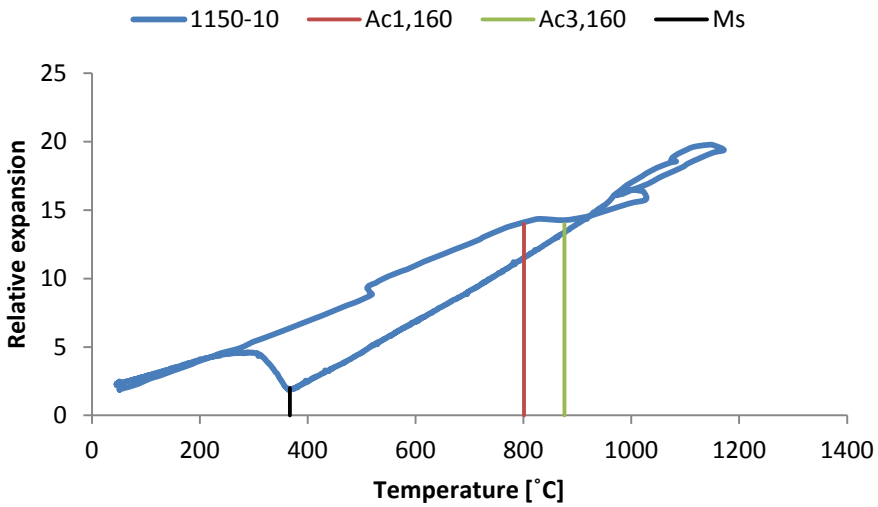

Figure 4-23: Dilatometer curve of sample quenched at 10 ˚C/s.

Upon cooling at 10 ˚C/s, M_s is observed at 367 ˚C, Figure 4-23. The smooth linear section of the dilatometer curve upon cooling until M_s is reached implies no bainaite has transformed. However, the HV10 values from Table 4-2 imply that there may be some bainite transformed due to a softer structure compared with the sample cooled at 60 ˚C/s. Also the structure

quenched at 10 ˚C/s has experienced temperatures above 600 ˚C for 39 seconds compared to the rapidly quenched specimen which was subjected to the same high temperatures for only 12 seconds, which may have led to a higher degree of recrystallization.

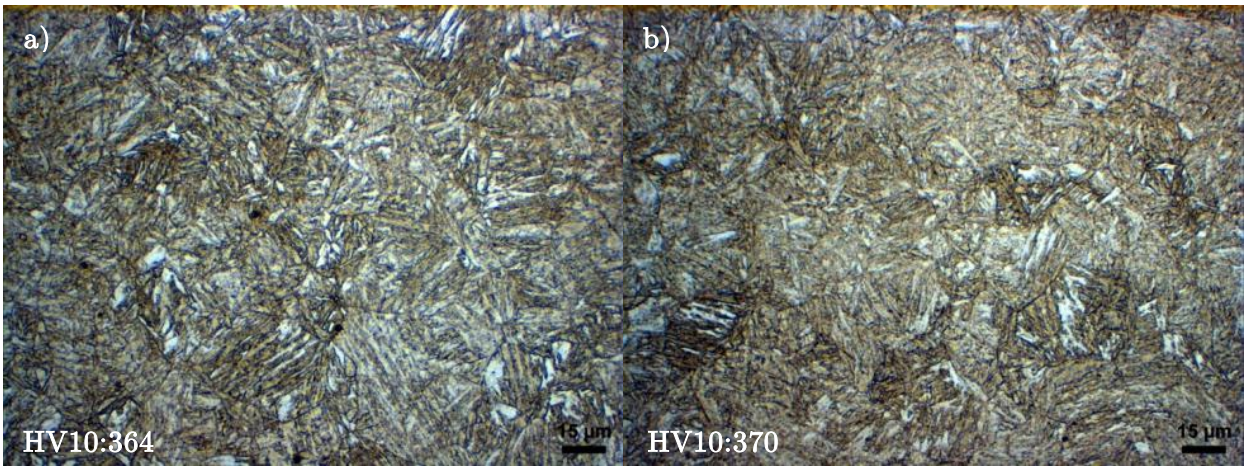

Figure 4-24: Microstructure after tempering: a) 1150-60-680-1 b) 1150-10-680-1

After only one second of heat treatment a significant hardness reduction can be observed from Figure 4-24. A finer martensite structure is achieved and outlines of the old austenite grain boundaries are observed at both quenching rates. After some tempering, the quenching rate does not affect hardness values significantly. Some recovery is expected to have annihilated a certain fraction of sub grain boundaries creating a more coherent interface between the laths.

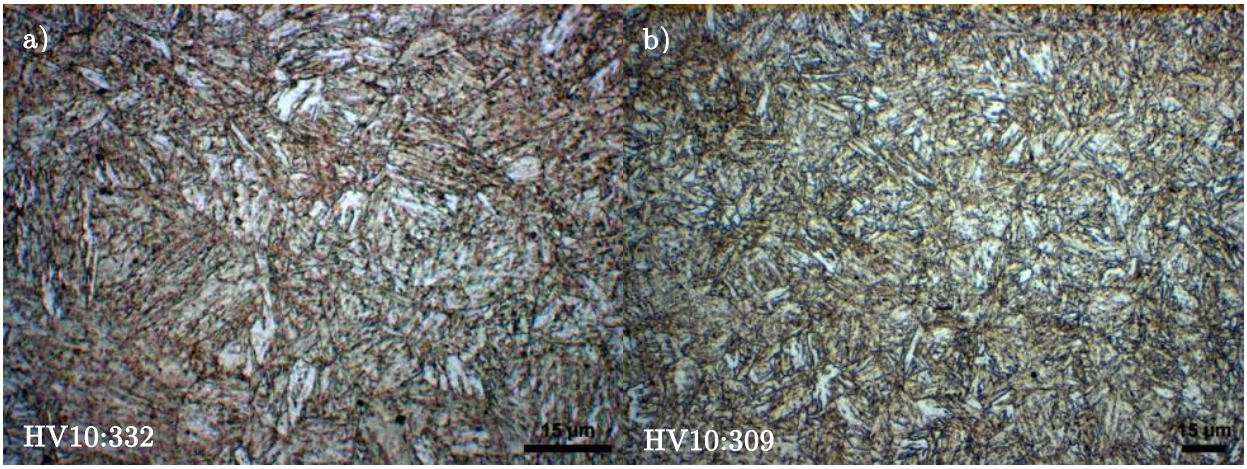

Figure 4-25: Microstructure after tempering: a) 1150-60-680-300 b) 1150-10-720-300

Several particles are observed after five minutes of tempering, Figure 4-25. Some recovery has occurred and the laths have taken a more acicular morphology and hardness values have decreased.

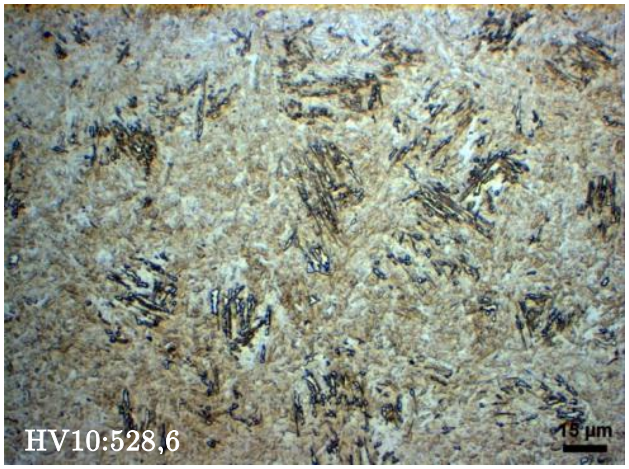

Figure 4-26: Microstructure after tempering: 1150-60-735-300

From Figure 4-26 it is evident that the structure has been subjected to temperatures in the two phase region during heat treatment. The dark martensite patches are remnants from the structure obtained after quenching. The brighter areas are newly formed martensite which have transformed upon cooling after tempering. The high HV10 values also suggest a high fraction of untempered martensite.

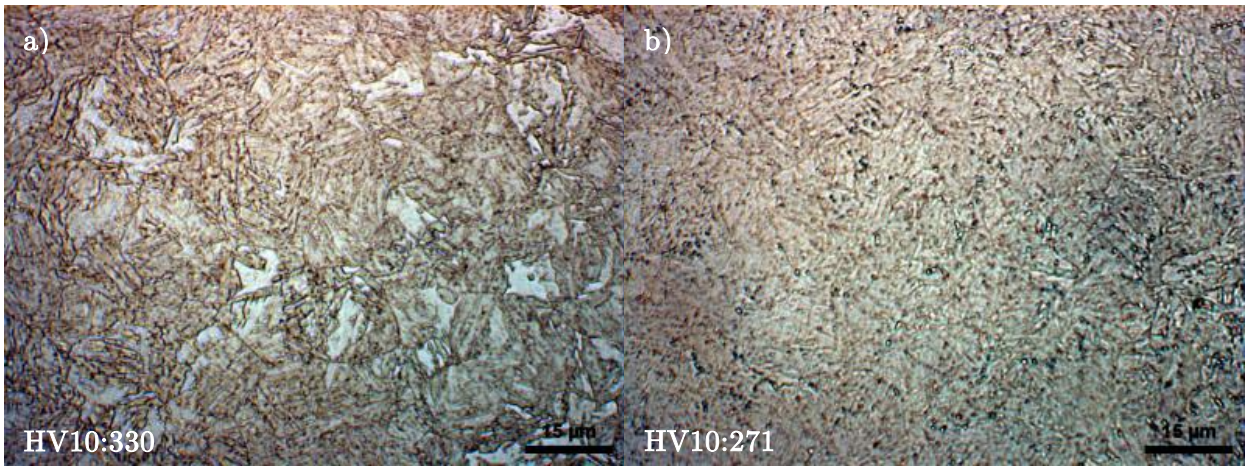

Figure 4-27: Microstructure after tempering: a) 1150-60-680-1200 b) 1150-60-720-1200

Tempering for twenty minutes has reduced the hardness furthermore and the lath boundaries are less distinguishable. Some larger particles can also be observed in the structure presented in Figure 4-27.

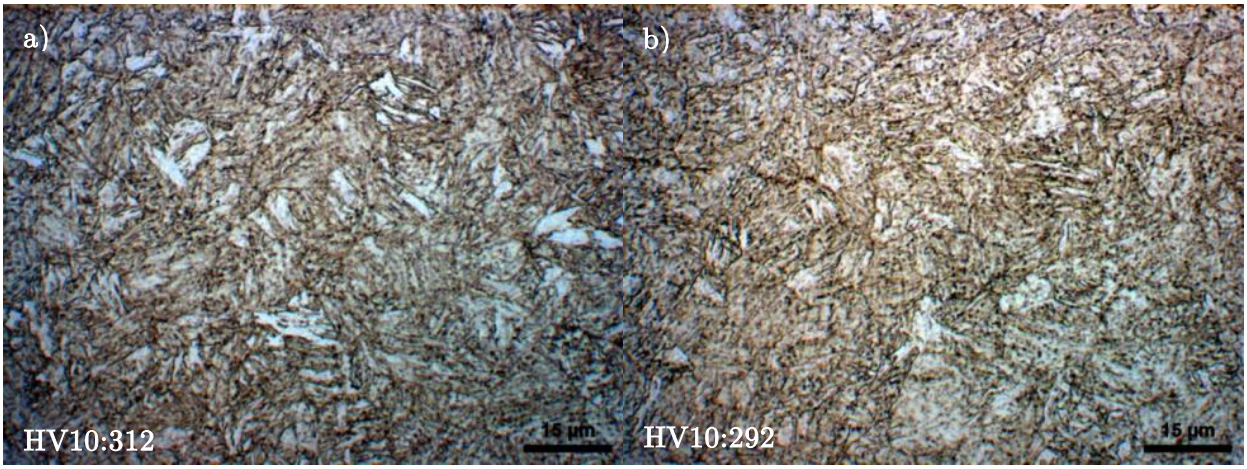

Figure 4-28: Microstructure after tempering: a) 1150-60-680-3600 b) 1150-60-720-3600

From Figure 4-28 the structure exhibits many of the same features after one hour of furnace tempering as observed at lower tempering times. Hardness is higher in the case of tempering at 720 ˚C compared to the corresponding samples at twenty minutes. This observation will be further addressed in Section 5.

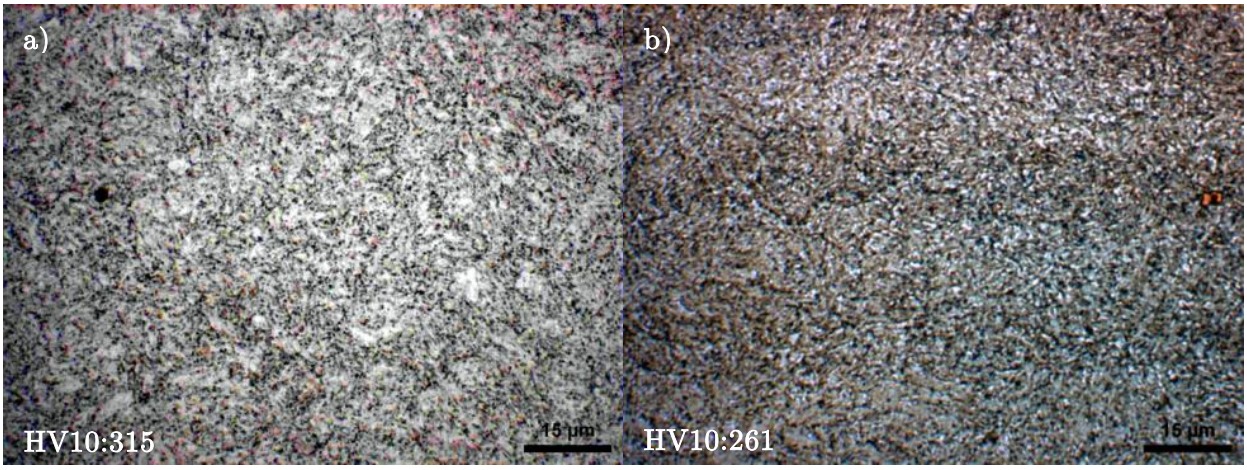

Figure 4-29: Microstructure after tempering: a) 1150-60-680-10800 b) 1150-60-720-10800

After three hours of tempering the structure is recrystallized and contains a large number of course particles as can be seen from Figure 4-29. Hardness is low, implying a low hardening contribution from the carbides.

4.6.2 Microstructure of Intercritical (IC) zone – initial tests

The microstructure obtained after heating in the two phase region followed by quenching is dominated by old martensite for both cooling rates. Figure 4-30 a) shows small islands of newly formed martensite, but these features are not easily observed in a). The structure in Figure 4-30 b) has been exposed to the high temperature range slightly longer than a) due to the lower quenching rate which may have led to a higher degree of recrystallization.

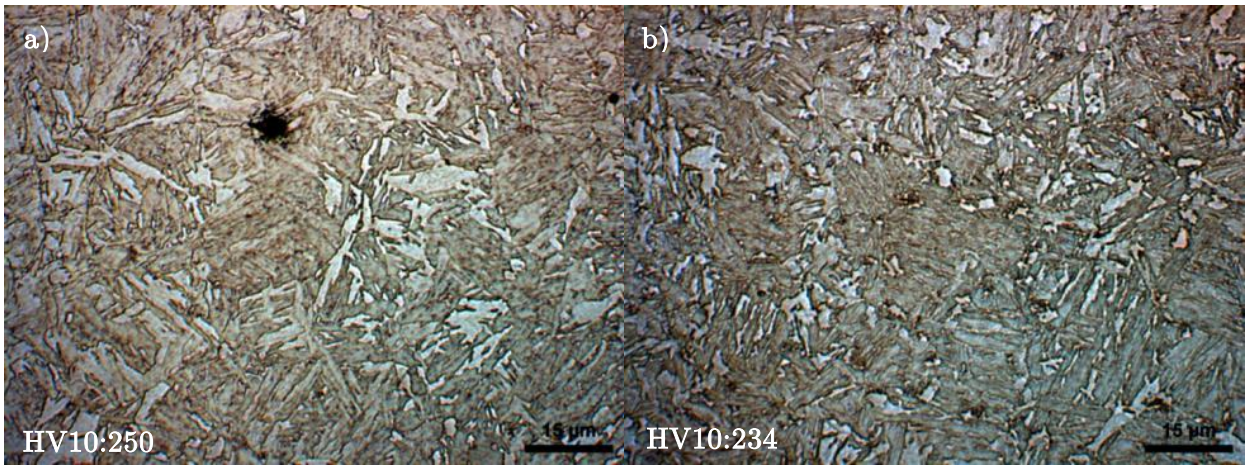

Figure 4-30: Microstructure of IC zone subjected to a Tpeak of 800 oC: a) 800-60 b) 800-10

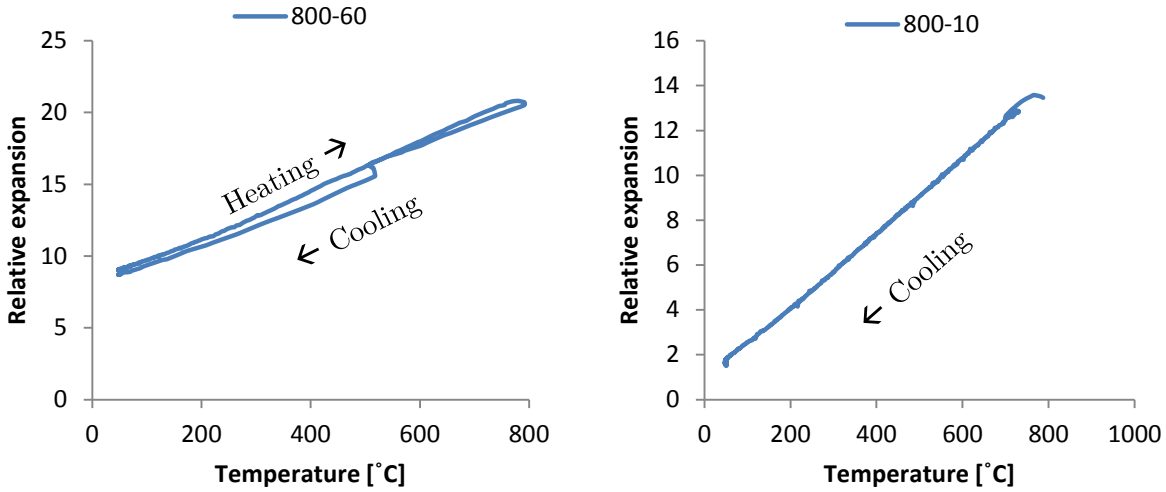

Figure 4-31: Dilatometer curves of sample heated to 800 ˚C: a) 800-60 b) 800-10

The dilation curve from Figure 4-31 a) shows no transformation during cooling, implying that the phase transition has not taken place upon heating. Figure 4-31 b) does not show any linear deviation upon cooling, i.e. no phase transformation. The microstructure images and the

hardness values from Figure 4-30 suggests that some transformation may have occurred, but has not been confirmed by the dilatometer.

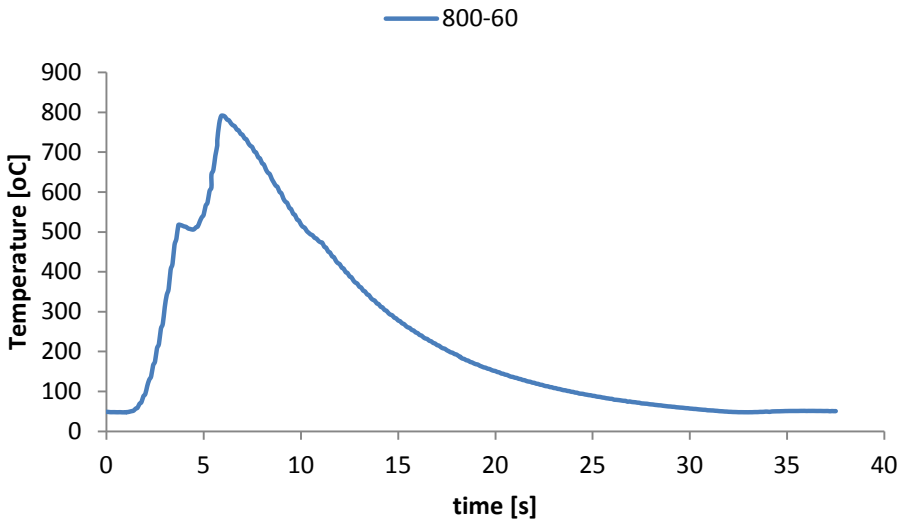

Figure 4-32: Typical heating cycle of sample heated to 800 ˚C: 800-60

Figure 4-32 presents the temperatures measured by the thermo elements upon heating to 800 ˚C followed by quenching.

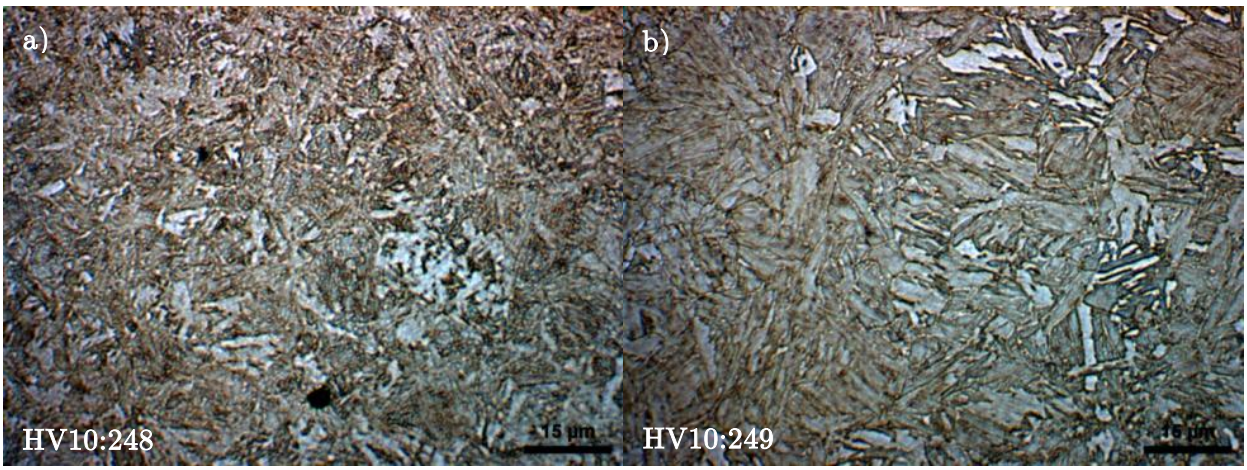

Figure 4-33: Microstructure of IC zone subjected to a Tpeak of 750 ˚C: a) 750-60 b) 750-10

After heating to 750 ˚C followed by quenching, the microstructure is stillmainly martensite, as can be seen from Figure 4-33. Small traces of newly formed MA phase can be observed on some of the old austenite grain boundaries as dark strips or beads.

4.6.3 Microstructure of the Inter Critical (IC) zone – model approach

The microstructural images were taken 2.7 mm from the weld center on the samples subjected to tempering. The images of the un-tempered samples in Figure 4-34, are taken 3 mm from the weld center and shows a mixture of former tempered martensite (light colors) and newly formed MA phase (dark colors).

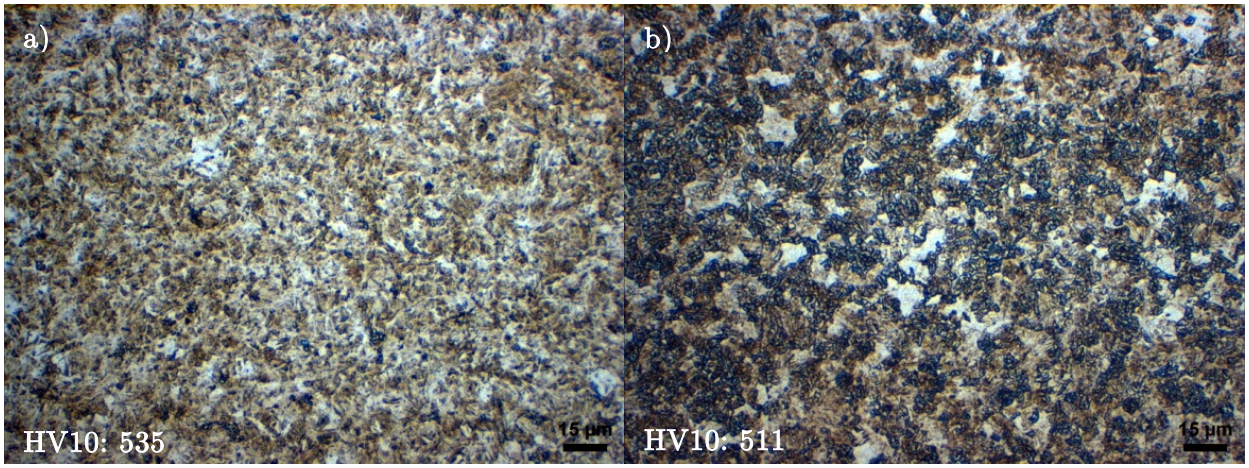

Figure 4-34: As quenched microstructure 3 mm from weld center: a) 1150-60 b) 1150-10

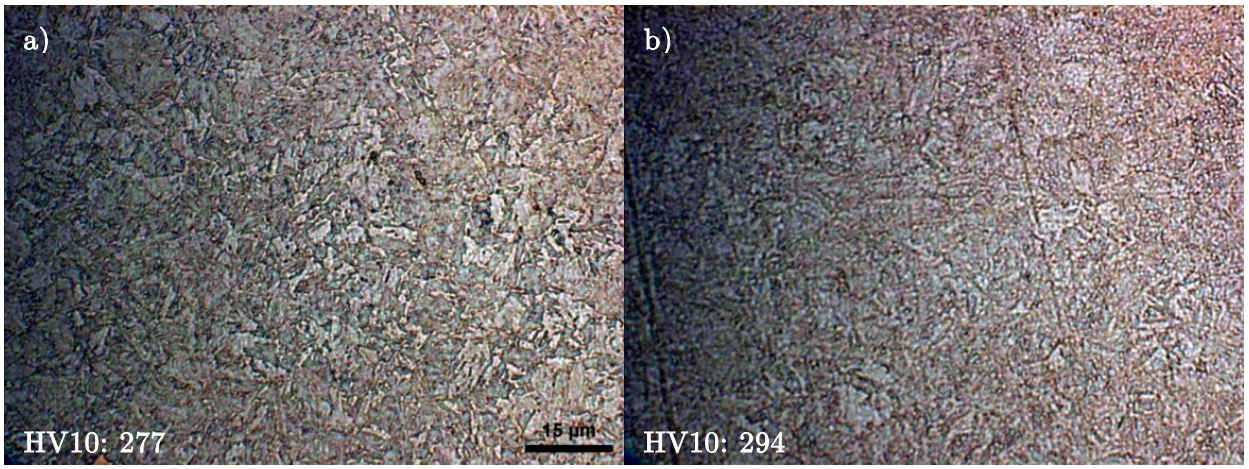

Figure 4-35: Microstructure of IC after tempering: a) 1150-60-720-3600 b) 1150-10-720-3600

After one hour of tempering the MA phase is no longer recognizable and the structure is softened considerably, Figure 4-35. The microstructure after three hours of tempering consists of a high fraction of particles dispersed in a soft recrystallized matrix which is seen from Figure 4-36.

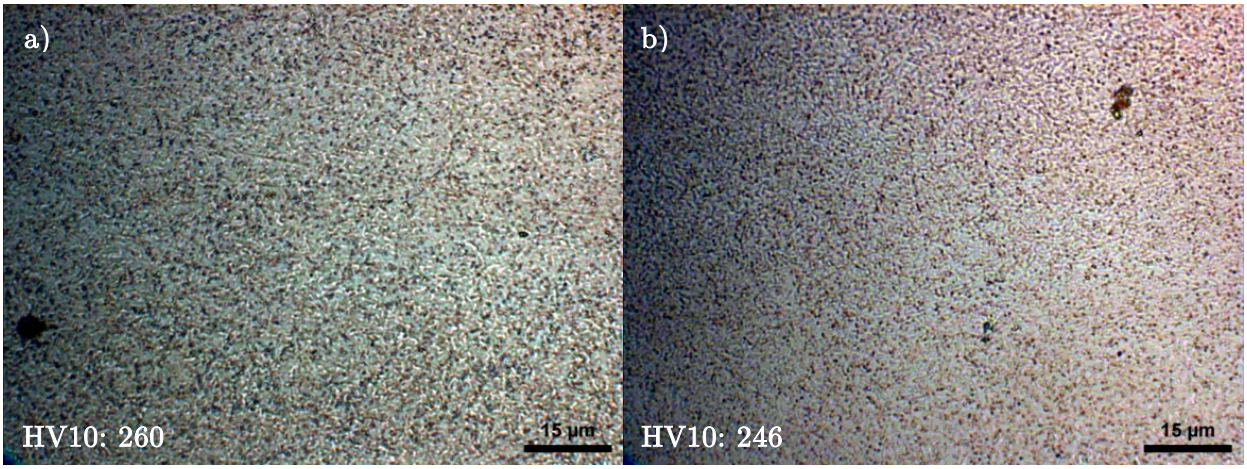

Figure 4-36: Microstructure of IC after three hours of tempering: a) 1150-60-720 b) 1150-10-720

4.6.4 TIG weld performed on C90 steel by FMC Technologies

The welding procedure performed by FMC Technologies is conducted using a TIG welding technique, where the weld is being built up by several layers, one for each weld cycle. The microstructure close to the bevel consists of a mixture between base material and the additives provided by the weld rods. The microstructure in the vicinity of the bevel where additives were no longer observed is presented in Figure 4-37. After welding is complete, the heat affected zone is tempered at a temperature between 690-700 ˚C for six hours.

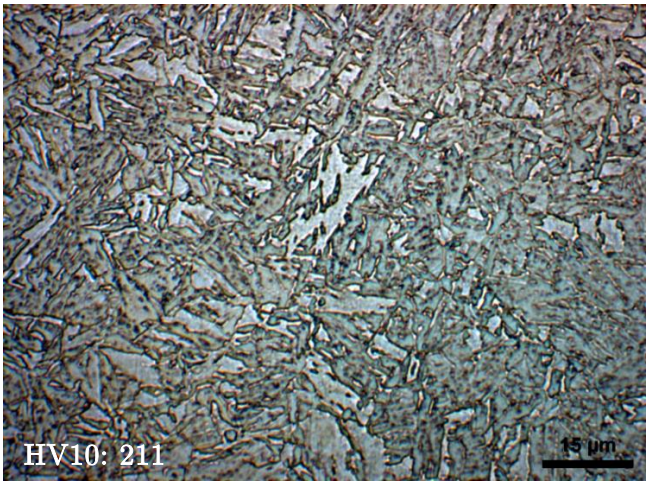

Figure 4-37: Microstructure of C90 5 mm from TIG weld bowel. Sample provided by FMC technologies.

Hardness measurements were performed on the TIG weld and the results are presented in Figure 4-38. The hardness values close to the bevel (x=0, x=1) have been made in the mixed structure of additives and base material, and hardness values are slightly higher in this region compared to

further out. A small hardness drop is observed in the interface between the structure containing additives and base material.

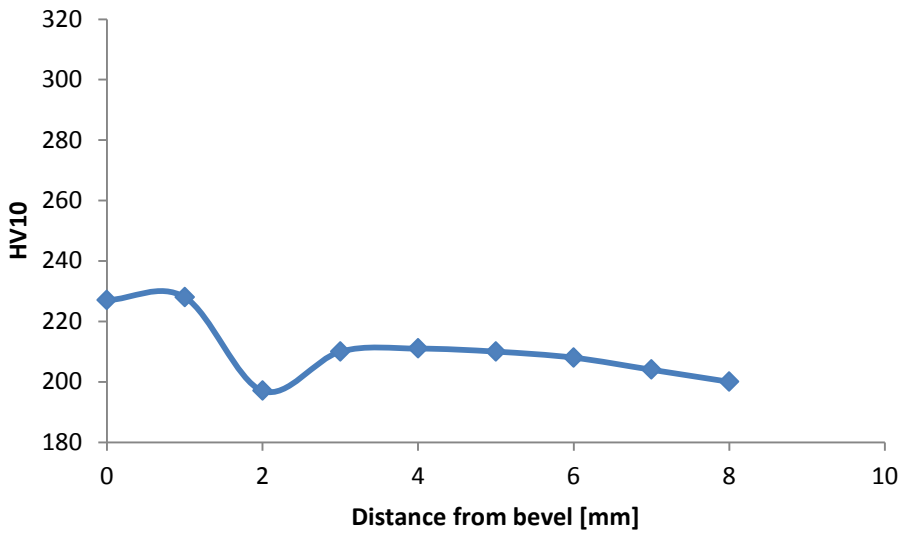

Figure 4-38: Hardness profile of HAZ in weld performed by FMC Technologies.

4.7 Fracture surface

4.7.1 SEM

SEM images were made from the fracture surfaces resulting from the impact toughness testing. Images were taken on both macro –and microscopic scales. In this section the figures are labeled with numbers from 1-3, where 1 corresponds to the area at which the crack has been initiated. Images labeled with 2 and 3 are further away from initiation site, and is illustrated in the images of low magnification. Some selected images will be presented in this section.

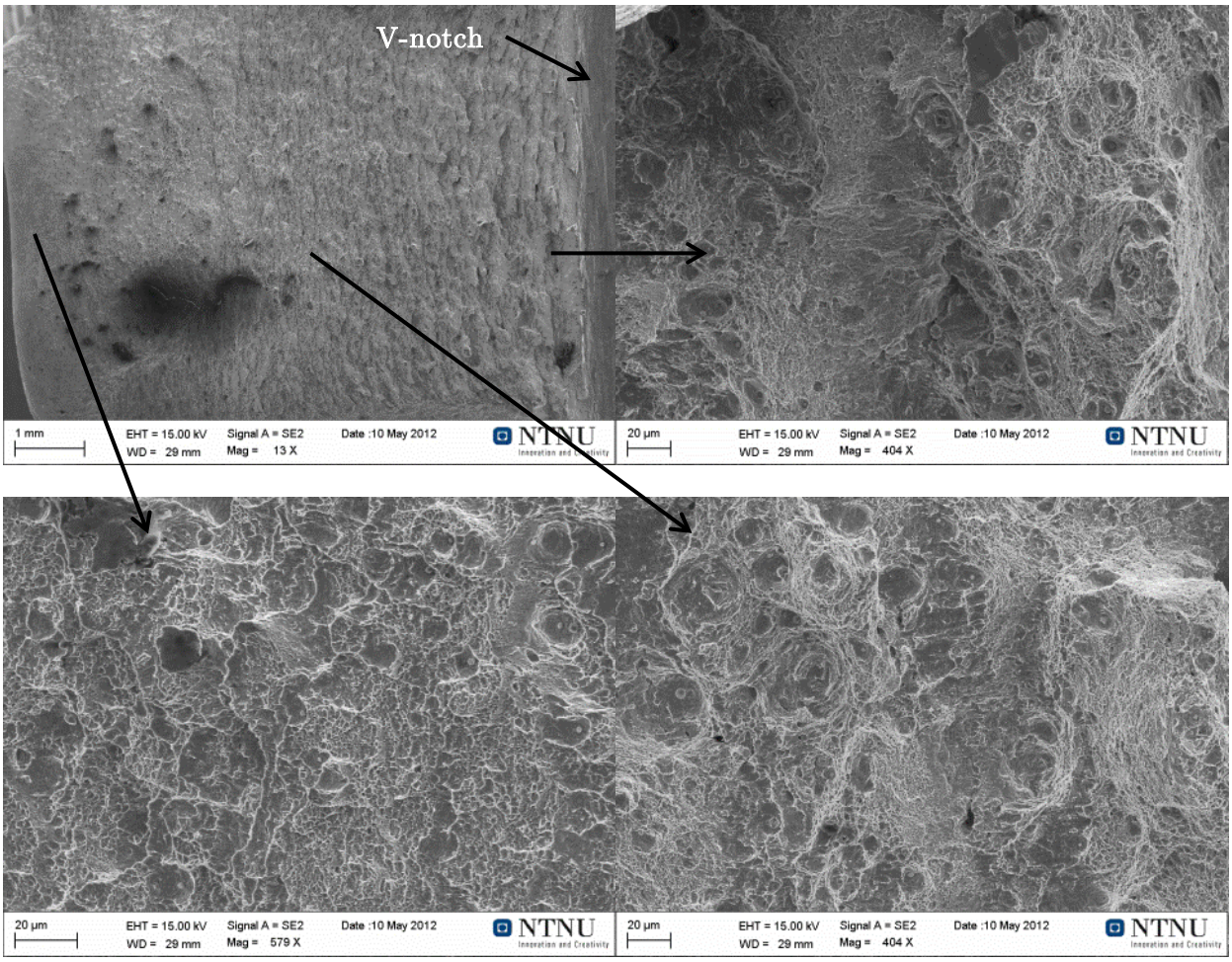

Figure 4-39: SEM of fractured surface of material with high impact toughness (139 J).

The fractured surface in Figure 4-39 is characterized by a high degree of topography implying substantial plastic deformation before fracture. The high magnification images reveal several dimples, some with visible particles remaining from where the deformation initiated. As the fracture progresses through the cross section, topography and deformation decreases slightly.

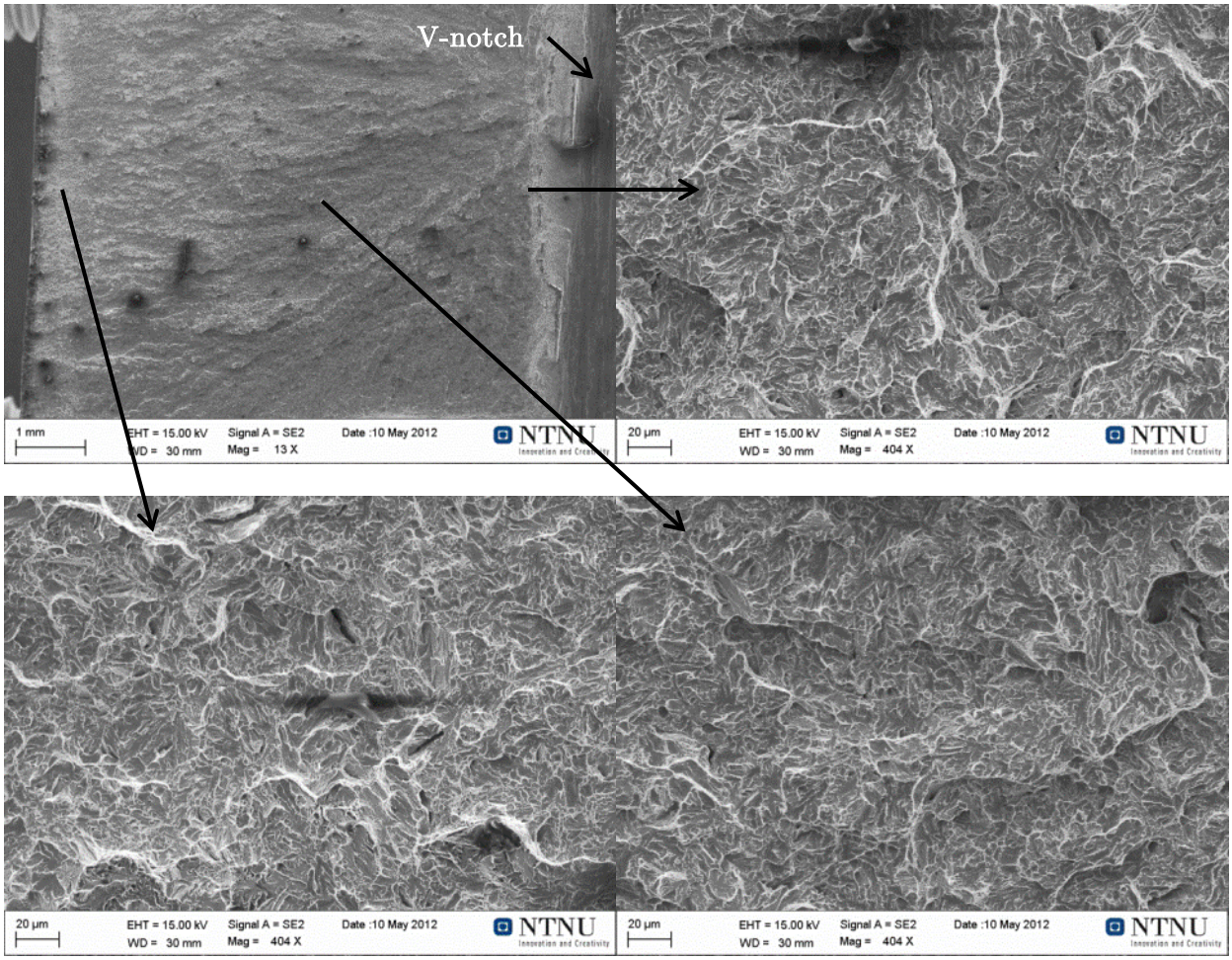

Figure 4-40: SEM of fracture surface of material with poor impact toughness (32 J).

Figure 4-40 shows a fracture surface of poor impact resistance and is characterized by little deformation and topography. From the overview image it is evident that the crack has initiated at some local stress concentration and propagated from this point. The images with high magnification show a mixture of ductile and brittle fracture. Little or no dimpling has occurred and large obstacles can be seen at the center and to the left of the fractured specimen's cross section. The low degree of deformation is supported by the low variation in brightness and contrast with the exception of the large obstacles.

4.7.2 Light microscopy and hardness

A sample from the parallel tempered in Smitweld for 20 minutes at 720 ˚C (1150-60-720-1200) was subjected to further investigation due to low impact resistance. The selected parallel is presented with a letter (in this case "b"), which can be corresponded to the impact toughness results obtained for this exact sample and can be found in Appendix B: Complete Charpy V chart. The fractured surface was grinded down and polished, before subjected to analysis and is presented in Figure 4-41.

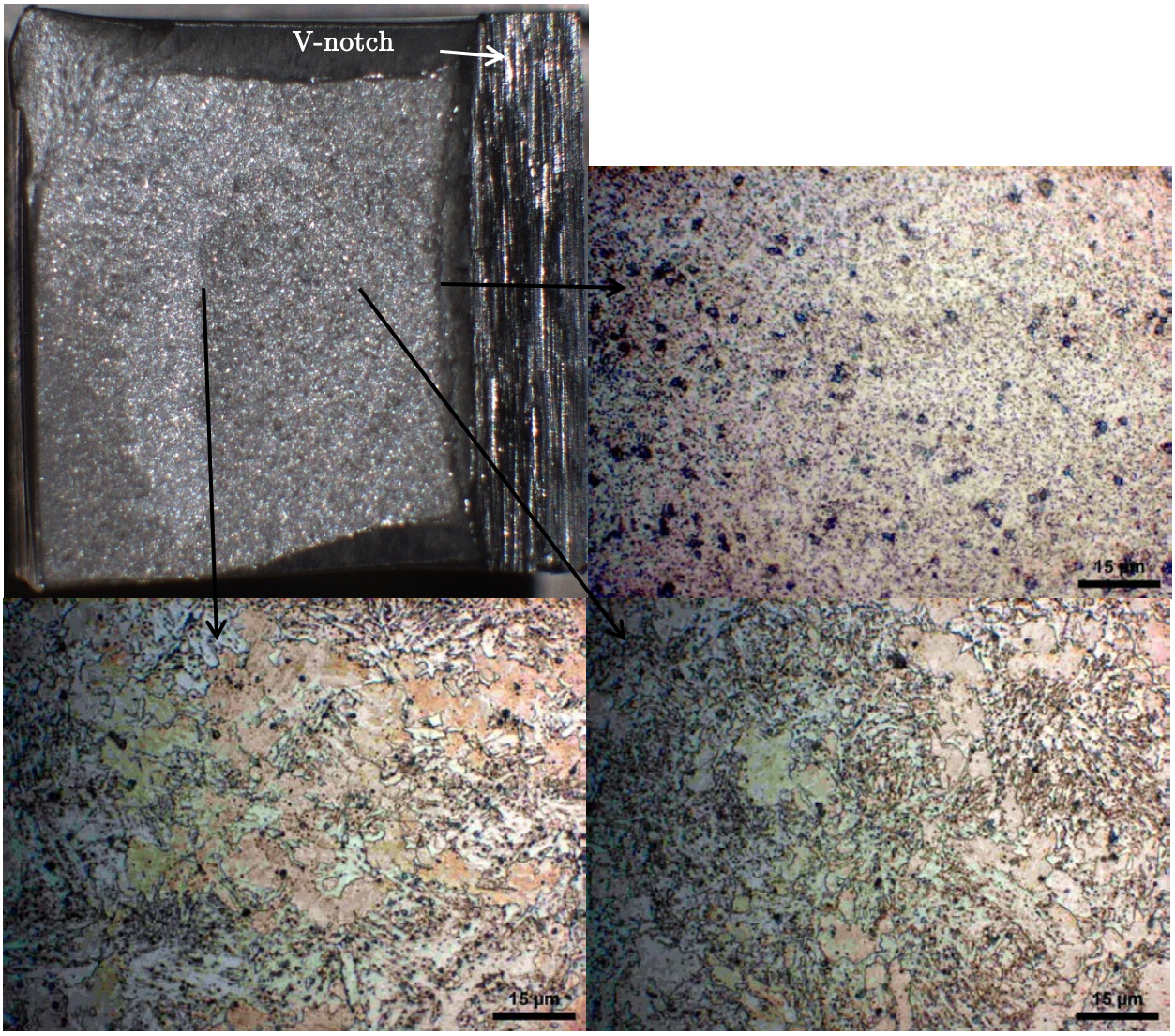

Figure 4-41: Fracture surface. High mag. images are taken at 0,5, 2 and 5 mm from V-notch. Sample parallel: 1150-60-720-1200 b.

From Figure 4-41, martensite formed upon cooling after tempering is observed some 2 mm from the V-notch and the amount increases further into the cross section. Hardness measurements

were performed on the same cross section and are presented in Figure 4-42: The Vickers hardness values support the microstructure evaluation which suggests a martensitic structure deeper in the cross section.

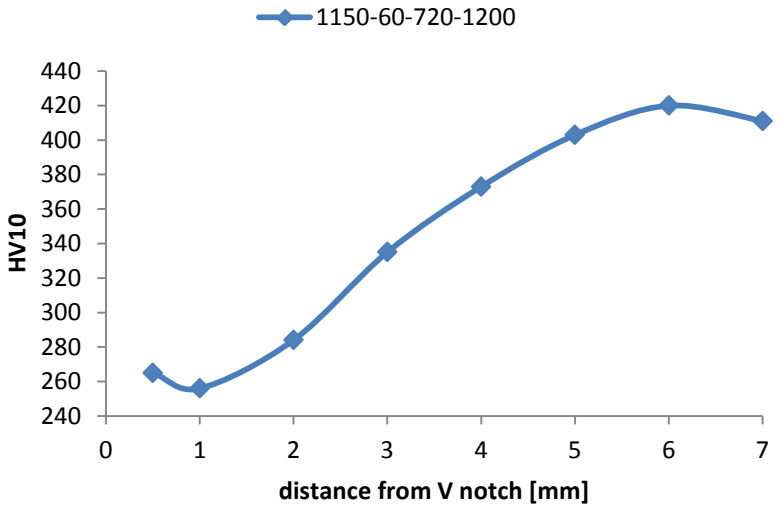

Figure 4-42: Hardness measurements of fractured cross section. Parallel: 1150-60-720-1200 b.

A similar test procedure was performed on one parallel furnace tempered for three hours at 720 ˚C and its cross section hardness profile in the fractured zone is presented in Figure 4-43. The furnace tempered sample showed no sign of any coarse and brittle new formed martensite.

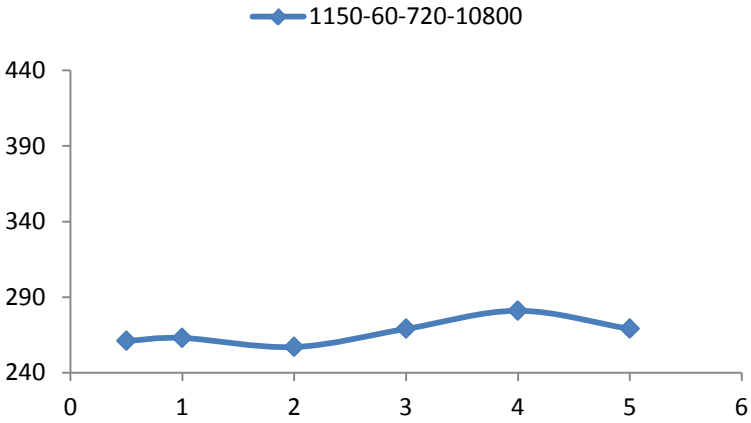

Figure 4-43: Hardness measurements of fractured surface cross section. Parallel: 1150-60-720-10800 b

5 Discussion

5.1 Weld hardness and impact toughness

The main experimental challenge of this work has been reducing the hardness of the weld to sufficiently low values. According to FMC Technologies and ISO, the weld cannot exceed 25.4 HRC (≈ 270 HV10) due to stress corrosion issues. The requirement for impact toughness is an average of 40 J from three parallel samples, with a minimum single result of 30 J. The C90 steel is a QT steel, meaning it is already in a tempered state prior to welding. Upon heating to temperatures above Ac3 the tempering effect is immediately lost and a structure of brittle and hard martensite forms upon rapid cooling. Tempering for just one second at 680 ˚C softened the weld by up to 33 % for the samples quenched at 60 ˚C/s and 27 % for the 10 ˚C/s cooling rate. The course bundles of lath martensite observed post quenching was significantly refined during the rapid reheating to 680 ˚C (Figure 4-24). By tempering at 720 ˚C for 20 minutes in the Smitweld apparatus, hardness values close to the requirement were obtained. However, when heat treatment was performed in a furnace at the same temperature, sufficient low hardness values was first reached after three hours of tempering. The implications of the different tempering effects observed by heat treatment in Smitweld and furnace will be discussed in Section 5.1.3.

5.1.1 Cooling rates

Two different cooling rates were applied on the weld simulated specimens, 10 and 60 ˚C/s. The controlled quenching temperature was activated when the sample reached 920 ˚C after it had been exposed to peak temperature of 1150 ˚C in order to reduce grain growth. Samples not subjected to tempering showed that the microstructure which had the higher quenching rate (60 ˚C/s) possessed the greater hardness value compared with quenching at 10 ˚C/s. This may be explained by some bainite formation for the lower quenching rate. However, there is no deviation in the dilatometer cooling curves which indicates that bainite has not developed. The specimens cooled with the lower cooling rate have been subjected to temperatures above the point at which recrystallization occurs (≈ 600 ˚C) for a longer period of time, 39 s compared with 12 s which may have resulted in a more course grained austenite. The impact toughness should be assumed be poorer at lower cooling rates, but there seems to be no such correlation from the Charpy V results obtained for tempering times above 300 s. From the microstructure images it is hard to outline the former austenite grains, but from Figure 4-24 the grains appear to be larger for the slower cooling rate.

5.1.2 Tempering temperature and time

Three different tempering temperatures were tested on the welded specimens and were chosen based on earlier experiences and on results obtained by the dilatometer experiment. Tempering

at 680 ˚C has proven to have a good softening effect on steels previously subjected to weld simulations and was therefore chosen. The Ac1 temperature was found to be 743 ˚C for a heating rate of 2.5 ˚C/min ($Ac1_{,0.03}$) and temperatures close to Ac1, 720 and 735 ˚C was chosen for heat treatment experiments in addition to 680 ˚C.

The highest temperature (735 ˚C) proved to be too high in order to keep a proper distance from the transformation temperature and high levels of newly formed martensite were found in the post tempered microstructure, implying tempering well within the two phase region (Figure 4-26). The results from hardness and impact toughness tests reveal a hard and brittle structure. Tempering at 735 ˚C was therefore discarded as an applicable temperature.

Heat treatment at 720 ˚C proved to provide the most effective hardness reduction of the weld center. Hardness values of 271 and 282 HV10 was obtained after tempering for 20 minutes in the Smitweld apparatus and after three hours of furnace tempering, the hardness was well below the requirements with values of 261 and 253 HV10. From Figure 4-27 b) a rough distribution of course particles can be observed among the fine lath martensite structure. The impact toughness tests on the samples tempered at 720 ˚C showed some quite deviating results, varying from an average of 193 to 43 J after twenty minutes at 10 and 60 ˚C/s, respectively. The dilatometer cooling curves does not show any sign of any phase transitions. The fracture surface of one of the Charpy tested samples exposed to tempering at 720 ˚C for twenty minutes (1150-60-720-1200) was investigated further and microstructure analysis and hardness measurements of the fracture surface revealed that the structure in the vicinity of the thermocouples exhibited a low hardness value and a tempered martensitic structure. Tests performed closer to the center of the cross section of the sample, showed that newly formed martensite was present and the amount increased towards the opposite side from which the thermocouples stood (Figure 4-41). Based on the observed microstructure and hardness values (Figure 4-42) it is evident that a relatively large temperature gradient have been present over the specimen cross section, which may have been caused by poor contact between the sample and clamps during tempering. The hard and brittle untempered martensite structure observed explains the low impact resistance of this parallel and the Charpy results hold little value as the tempering temperature have been higher than the experiment design parameters for a relatively large fraction of the cross section. The Charpy results from the parallel quenched at 10 ˚C/s shows a very high impact resistance, and it is therefore assumed that these samples have not exceeded Ac1 at any point through the cross section. These results are therefore assumed to be more reliable than the 1150-60-720-1200 parallel, with respect to the real tempering effect at 720 ˚C.

After three hours of furnace tempering at 720 ˚C the hardness values are within the requirement, but impact toughness values are deviating and with high standard deviation as presented in

Table 4-5. Hardness values over the cross section remains stable, and no new formed martensite was observed. The relatively low Charpy values may be a result of tempering embrittlement. Unfortunately, no more samples were available for further testing.

Heat treatment performed at 680 ˚C showed a significant increase in impact resistance as can be seen from Figure 4-19. After three hours an average Charpy value of 224 J was found for the specimens quenched at 10 ˚C/s and 187 J for samples quenched at 60 ˚C/s. The hardness reduction due to tempering is lower compared to the specimens subjected to tempering temperatures of 720 ˚C, and has not reached sufficiently low values to meet the requirements with the chosen experimental parameters.

5.1.3 Smitweld vs. furnace tempering

Tempering was conducted in both the Smitweld apparatus and in an air circulating furnace. Due to the high costs of using the Smitweld, tempering for longer than twenty minutes was performed in the furnace. Some interesting observations regarding hardness evolution was found when comparing the two methods. Tempering aided by Smitweld caused the samples to soften at a higher rate than what was observed for the other samples. For one hour tempering in the furnace, an increase in hardness was observed in three of four parallels compared with the twenty minutes tempering performed in Smitweld. The main difference between furnace and Smitweld tempering is in the heating rate of the steel bar. The Smitweld apparatus heats the steel at up to 160 ˚C/s and reaches the preset temperature within a matter of seconds. The thermocouple readings from a furnace tempered bar (Figure 4-7) revealed that peak temperatures of 680 and 720 ˚C was not reached until 16 and 22 minutes had passed.

When the steel is heated to temperatures above 1050 ˚C no Mo, Fe or Cr carbides remain stable, forcing the elements back to solid solution which can be seen from Figure 2-9. Upon slow reheating, carbides such as ε-Fe_2C_4 will precipitate in the low temperature region. Due to the low temperature, the diffusion length will be short leading to a fine distribution of small particles in the martensite matrix. As temperature increases cementite nucleates at the ε- carbides and grows at their expense and will eventually coarsen. When temperatures reaches 700 ˚C, large carbides binding several alloying elements such as Cr and Mo (and Fe), will nucleate according to the C-Cr-Fe-Mo phase diagram presented in Figure 2-8, if given enough time. It should be mentioned that the presented phase diagram operates with a slightly higher carbon composition than what is present in the C90 steel (0.35 wt%), but will be applied for the sake of argument in this case. If these carbides nucleate at the old carbide sites, the structure can be suspected to contain a relatively fine distribution of carbides contributing to particle strengthening of the material. A pinning effect on the migrating grain boundaries may also reduce softening somewhat if the carbides are small and numerous enough. The small amounts of alloying

elements in the composition may be a limiting factor with respect to carbide size. Some solid solution strength will be lost due to the precipitation, but the effect may be annihilated by the contribution of the particles.

The Smitweld apparatus heats the steel at a very high rate (160 ˚C/s) and some of the tempering steps described in chapter 2.6 may not have been able to materialize due to the short heating time. At the point when the tempering temperature is reached, it is possible that only a few carbides have been given enough time to precipitate during the rapid heating. If that is the case, carbides of the type Fe_3C and $M_{23}C_6$ may start to nucleate unaffected by the low temperature carbides. At high temperatures, diffusion lengths are significantly increased and may result in a distribution containing fewer and larger carbides. The solid solution strengthening will decrease due to alloying elements being bound by the carbides, and yet the carbides may be too coarsened and far apart to contribute noteworthy to precipitation strengthening.

A graphic presentation of the proposed explanation is presented in Figure 5-1 and Figure 5-2. Note that the time scales in these two figures are not the same.

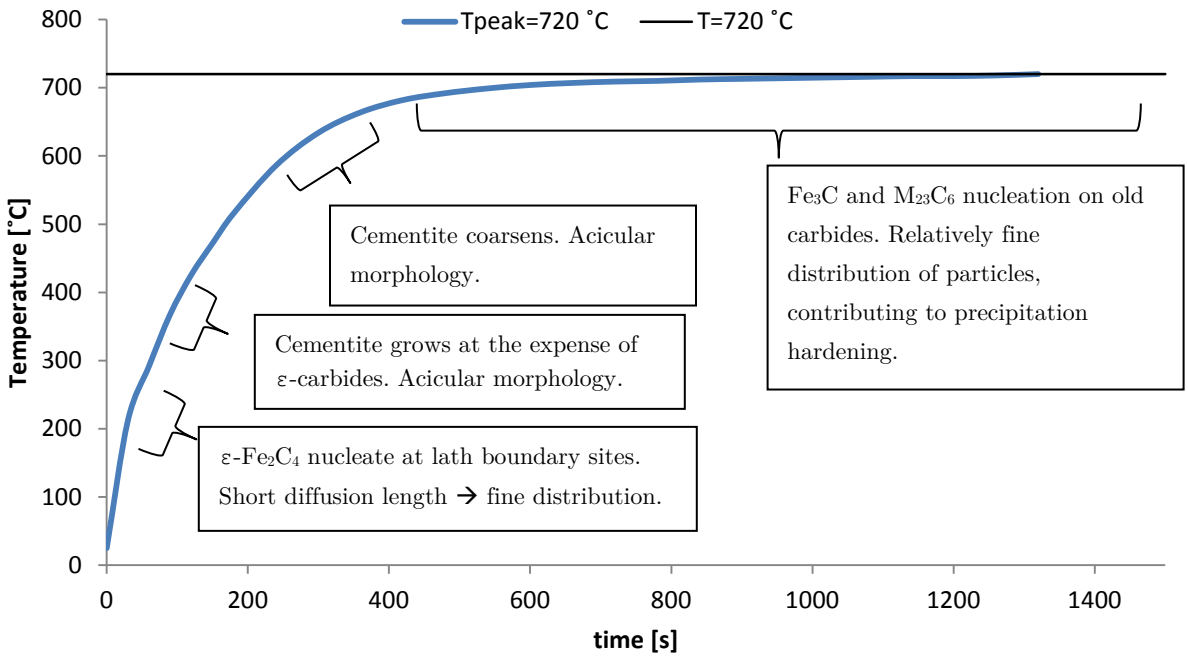

Figure 5-1: Possible tempering mechanisms upon slow heating.

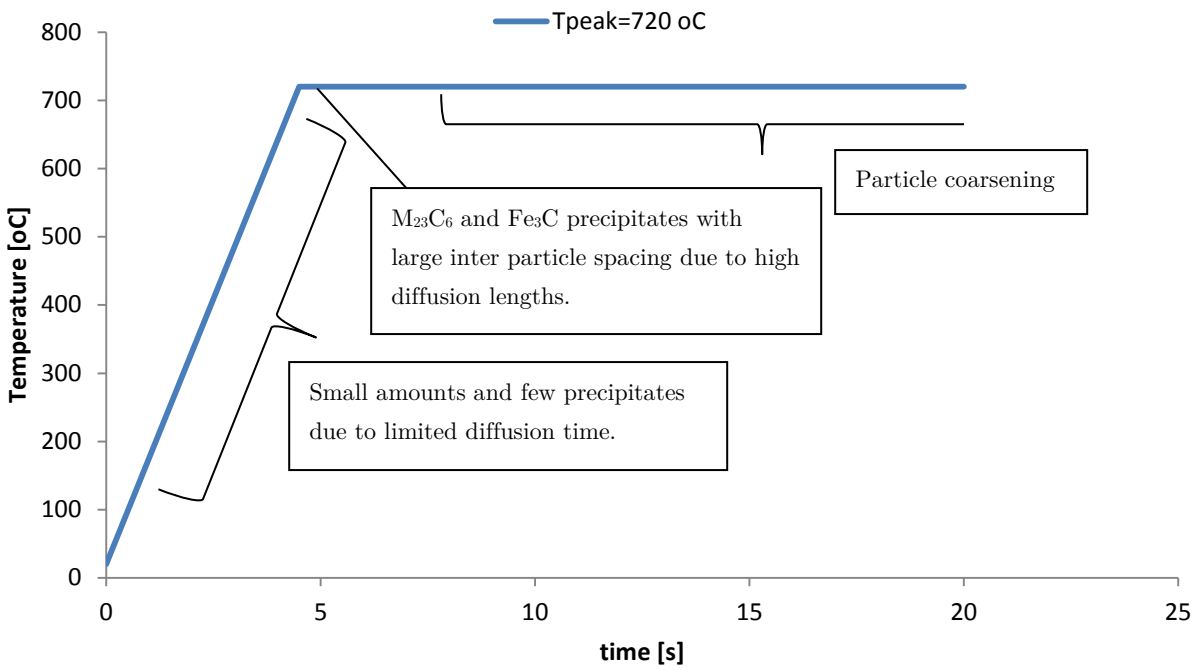

Figure 5-2: Possible tempering mechanisms upon rapid heating.

When comparing the microstructure images from Figure 4-28 b) and Figure 4-27 b) there appears to be a finer particle distribution after furnace tempering for one hour than what is observed in the Smitweld tempered specimen.

If it so, that rapid heating to the tempering temperature softens the structure more efficiently than conventional furnace heating does, hardness values meeting the requirements could be achieved well before three hours. Due to high costs and material shortage, no samples were subjected to ohmic heating for longer than 20 minutes.

5.2 Intercritical zone

The intercritical (IC) study has been approached from two different perspectives and involves subjecting the microstructure to peak temperatures in the two phase region upon weld simulations. First, samples were heated to some pre-selected temperatures (750 and 800 ˚C) above the Ac1 temperature obtained from the dilatometer experiment ($Ac1_{,0.03}$) presented in Section 4.2, before quenching at 10 and 60 ˚C/ followed by furnace tempering at 680 ˚C for 0, 3600 and 10800 seconds. According to dilatometer readings, microstructure analyses and hardness values it is evident that these specimens did not enter the two phase region upon heating. For the weld simulated samples heated at rate of 160 ˚C/s, the austenite transformation

does not start until about 800 ˚C, which explains why very little MA phase was observed in the post heated specimens selected for this study.

Due to the unsuccessful first approach to the intercritical study, a second study was performed based on data obtained from the model presented in Figure 4-4 and dilatometer results from weld simulation (Figure 4-15). The $Ac1_{,160}$ is reached at 801 ˚C and $Ac3_{,160}$ at 876 ˚C. According to Figure 4-4, the temperature interval defined by the respective transformation temperatures is found 2.4-2.8 mm from the weld center. The selected temperature of 829 ˚C is found 2.7 mm from the weld center, which is where the microscopy and hardness tests were performed. The reference hardness value (no tempering) was calculated based on the average value found between 2 and 3 mm from the weld center before these samples was subjected to further tempering. After one hour of heat treatment at 720 ˚C the hardness readings of the intercritical zone was 24 and 7 HV10 above requirements and after three hours, both parallels were well below 270 HV10 with values in the range of 225-237 HV10 (Table 4-4).

5.3 Weld simulations vs. TIG

A weld performed by FMC Technologies on the C90 steel was provided. The weld cycle includes TIG welding followed by a six hour tempering session at 690-700 ˚C in order to meet hardness requirements.

Weld simulations in Smitweld followed by tempering shows that hardness and impact requirements can be reached within three hours, which is a reduction of 50 % compared to the weld procedure performed by FMC Technologies. After twenty minutes of tempering in the Smitweld apparatus, the weld center hardness was measured to 271 HV10 for the sample quenched at 60 ˚C/s. This may imply a significant reduction in post weld heat treatment time if the softening in a real case follows a similar course as shown from Figure 4-9. Comparing HAZ hardness profiles of TIG weld with weld simulations, a steady reduction in weld hardness is observed for the latter after three hour tempering. The TIG weld exhibits a hardness drop of 31 HV10 in the transition interface between material containing additives and base material, which can be seen from Figure 4-38. The local drop in hardness may have some effect on the local yield stress, but that issue has not been pursued further in this work.

5.4 Applicability to the SAG-FW process

The Solid Active Gas – Forge Welding procedure relies on ohmic heating of the pipe ends that are to be joined, whilst a protective agent (gas) is flowed through or flushed upon the mating pipes. The heating rate obtainable by this process is similar to the Smitweld apparatus, and the method should therefore be transferable at the weld center. Tempering of the weld in Smitweld is however, somewhat different as the peak temperature is only obtained at the center, meaning

sections further away along the length axis experiences lower temperatures. This is an issue not necessarily present in the SAG-FW process as broader induction coils can be applied, providing a more uniform temperature distribution over the heat affected zone. At the HAZ/base material interface, a softening course as seen in Figure 4-18 can be expected. It is suggested that the weld simulations performed in Smitweld is transferable to the SAG-FW process in the HAZ. When tempering is concerned, only the structure obtained at the weld center is suggested to be transferable due to the large temperature gradients observed over the HAZ by heat treatment in Smitweld. Furnace tempering is considered not to be transferable to the SAG-FW tempering method, because of the slow heating rates obtained by this procedure. Deformation upon mating of the pipes can result in local grain refinement, increasing the weld hardness. However, that is an issue not considered in this thesis.

6 Conclusion

Weld simulations have been performed on a C90 steel used for offshore riser systems. The test specimens were rapidly heated (160 ˚C/s) to 1150 ˚C and then quenched to room temperature at two different rates, 10 and 60 ˚C/s by applying a Smitweld Thermal Simulator apparatus. The welds were then subjected to tempering at different temperatures and durations. The weld must exhibit impact toughness above 40 J at -20 ˚C and have a Vickers Hardness (HV10) value of no more than 270, in order to meet requirements.

Weld hardness requirements was met after three hours of post weld heat treatment at 720 ˚C in an air circulating furnace, producing hardness values of 261 and 253 HV10 for the respective cooling rates of 60 and 10 ˚C/s. Average impact toughness results of 119 and 66 J were found for the corresponding parallels, though with a high standard deviation value. After some tempering, cooling rates did not affect hardness values significantly. A TIG welding procedure followed by tempering performed by FMC Technologies, requires six hours to obtain satisfactory weld properties. The results from the weld simulations in this work suggest that the overall tempering time consumption can be reduced with at least 50 %, by implying a solid state weld procedure.

Tempering in furnace proved to soften the material less efficiently than what was observed by applying the Smitweld apparatus. Samples tempered for twenty minutes at 720 ˚C in Smitweld showed a Vickers hardness of 271 HV10 whilst samples heat treated in a furnace for one hour at the same temperature, had a hardness value of 292 HV10. Both parallels were quenched at 60 ˚C/s.

The intercritical zone of the weld was softened to 260 and 246 HV10 for the two cooling rates (60 and 10 ˚C/s) after three hours of furnace tempering at 720 ˚C.

It has been suggested that the higher heating rates obtained in Smitweld retards or delays some of the low temperature tempering mechanisms, resulting in precipitation of coarse intermetallic carbides with relatively large inter particle spacing which contributes little to precipitation hardening. Upon slow heating, which is the case for furnace tempering, it is suggested that carbides precipitated at low temperatures exhibits a small diameter and a fine distribution. These precipitates may act as nucleation sites for the larger carbides expected to form at higher temperatures, producing a more finely distribution of smaller size carbides, which in turn contributes to precipitation hardening. Charpy results from samples quenched at 60 ˚C/s and tempered for twenty minutes, showed some local over heating in the structure subjected to impact tests, and the results are not considered reliable.

The weld simulations performed with Smitweld is likely to be transferable to the SAG-FW procedure as the two methods exhibits the ability to manage high heating and cooling rates. However, the obtained structure from Smitweld tempering is only transferable at the weld center. Furnace tempering has not been considered comparable to the SAG-FW process due to the significant difference in heating rates. .

7 Further work

To determine if a higher softening effect exists for tempering in Smitweld compared to furnace tempering, longer tempering times (>1200 s) could be carried out in the Smitweld apparatus. Reference samples tempered in furnace should then reveal if a significant difference in hardness reduction was obtained. Furthermore, Transmission Electron Microscopy (TEM) investigation performed on specimens tempered by the two methods may reveal difference in particle size, distribution and/or composition and help explain the observed difference in tempering effect.

Charpy V values of the 1150-60-720-1200 parallel were considered not to be reliable as some new formed martensite had transformed upon cooling from the tempering stage. A new test parallel should therefore be performed in order to determine the impact toughness of a structure not locally subjected to temperatures above Ac1 during tempering.

The applicability to the SAG-FW process, have in this work not taken account for the plastic deformation in the HAZ upon mating of the pipes. The plastic deformation will introduce several dislocations and might affect the degree of recrystallization, as the driving force for this mechanism is proportional to the dislocation density. In turn, this may lead to some grain refinement in the high temperature region, resulting in a harder post weld structure.

8 Bibliography

1. *FMC Technologies*. Available from: www.fmctechnologies.com.
2. Arnold, N. and S. Alexey, *Fundamental Concepts in Steel Heat Treatment*, in *Steel Heat Treatment*2006, CRC Press.
3. Raghavan, V., *C-Cr-Fe-Mo (Carbon-Chromium-Iron-Molybdenum).* Journal of Phase Equilibria and Diffusion, 2007. **28**(3): p. 270-273.
4. Garcı, et al., *Application of dilatometric analysis to the study of solid–solid phase transformations in steels.* Materials Characterization, 2002. **48**(1): p. 101-111.
5. Moe, P., et al., *Shielded active gas forge welding – from laboratory to field experiments.* International Journal of Material Forming, 2010. **3**(0): p. 1027-1030.
6. Thelning, K.-E., *Steel and its heat treatment*, 1984, Butterworth-Heinemann. p. 1-4.
7. Bhadeshia, H. and R. Honeycombe, *Steels*. Materials & Mechanical2006: Butterworth-Heinemann. 1-360.
8. Yokota, M. and G. Lai, *Toughness of lath vs plate M arten sites.* Metallurgical and Materials Transactions A, 1975. **6**(9): p. 1832-1835.
9. Babu, S., *Classification and Mechanisms of Steel Transformation**, in *Steel Heat Treatment*2006, CRC Press.
10. Solberg, J.K., *Teknologiske metaller og legeringer (Technological metals and alloys).* 2008.
11. *Stål och värmebehandling -En handbok (Steel and heat treatment - A hanbook)*2010: Swerea IVF.
12. Andrews, K.W., *Empirical formulae for the calculation of some transformation temperatures.* Journal of the iron and steel institute, 1965. **203**: p. 721-727.
13. Capdevila, C., F. Caballero, and C. Garcia de Andres, *Determination of Ms temperature in steels: A Bayesian neural network model.* ISIJ international, 2002. **42**(8): p. 894-902.
14. Lauralice, C. and T. George, *Hardening of Steels**, in *Quenching Theory and Technology, Second Edition*2010, CRC Press.
15. Grange, R., C. Hribal, and L. Porter, *Hardness of tempered martensite in carbon and low-alloy steels*. Metallurgical and Materials Transactions A, 1977. **8**(11): p. 1775-1785.
16. Speich, G. and W. Leslie, *Tempering of steel.* Metallurgical and Materials Transactions B, 1972. **3**(5): p. 1043-1054.
17. *E23-07ae1: Standard Test Methods for Notched Bar Impact Testing of Metallic Materials*. 2012 April 12, 2012; Available from: http://enterprise.astm.org/filtrexx40.cgi?+REDLINE_PAGES/E23.htm.

Appendix A: Dilatometer plots from Smitweld

In this appendix dilatometer curves obtained from the Smitweld apparatus will be presented. For samples subjected to tempering, only the tempering part of the heat cycle will be presented. The thermal history can be found from the series titles from all plots. Sections of the dilatometer curves are in most cases not smooth. This effect is due to the apparatus lack of adjusting the temperature properly throughout heating and cooling. The most important features are the $Ac1_{,160}$ and M_s, observed at around 800 and 380 ˚C respectively.

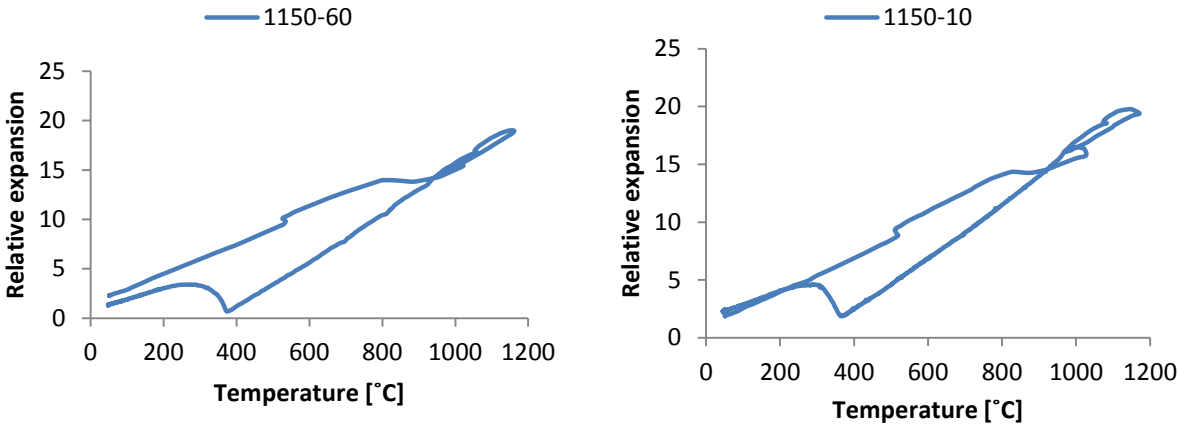

Figure 0-1: Dilatometer curves: Left: 1150-60 Right: 1150-10

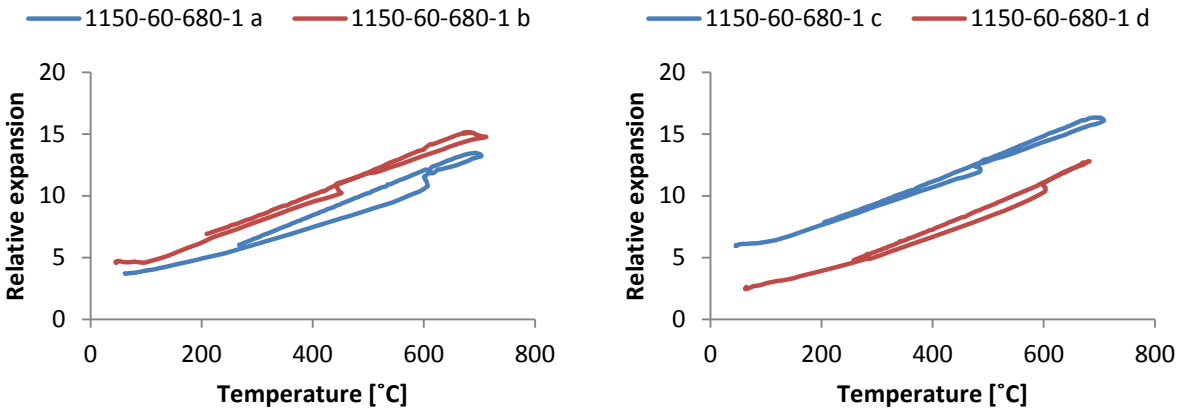

Figure 0-2: Dilatometer curves: 1150-60-680-1 a, b, c, d

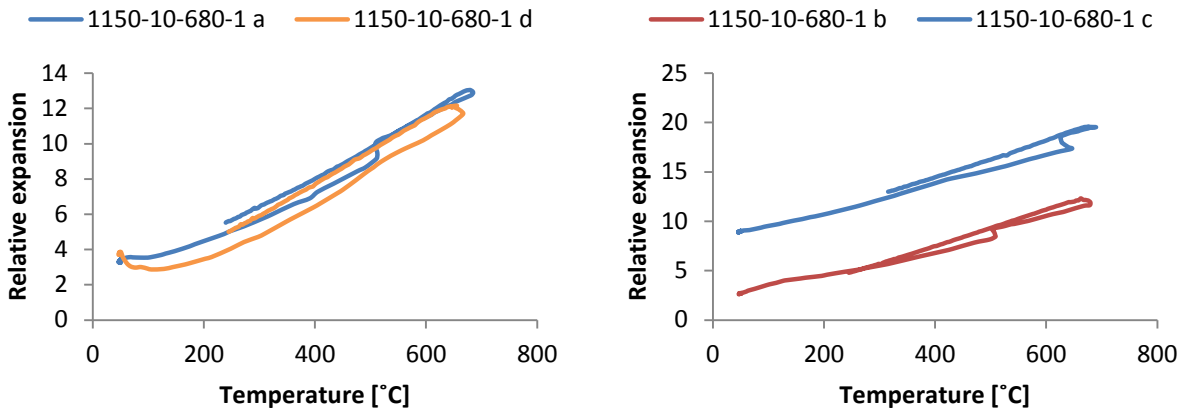

Figure 0-3: Dilatometer curves: 1150-10-680-1 a, b, c, d

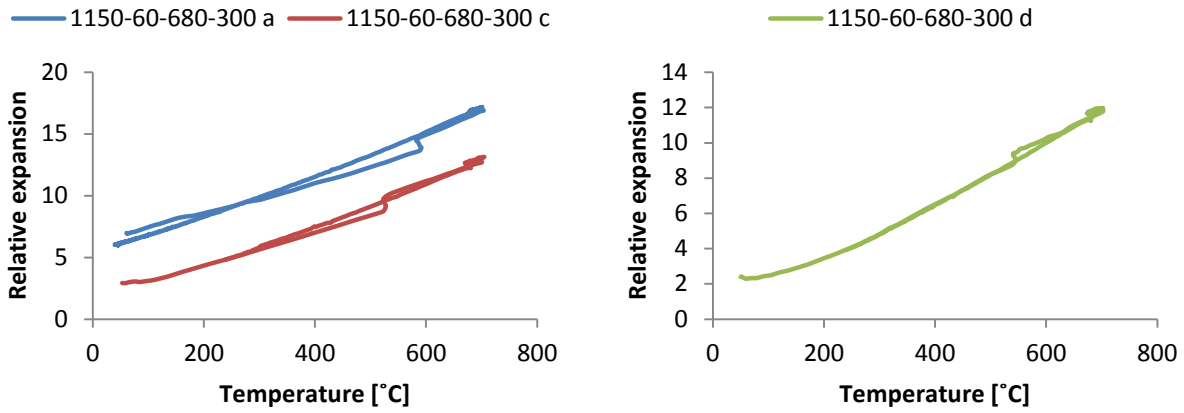

Figure 0-4: Dilatometer curves: 1150-60-680-300 a, c, d

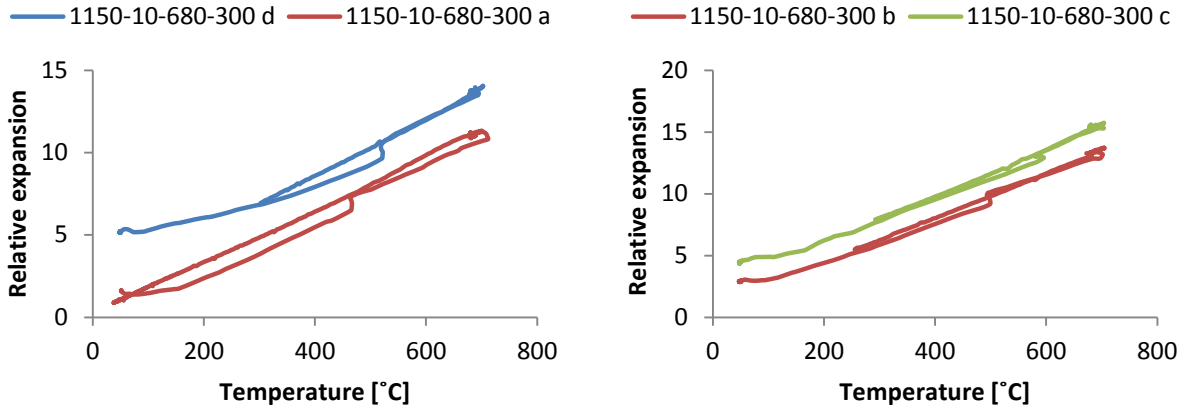

Figure 0-5: Dilatometer curves: 1150-10-680-300 a, b, c, d

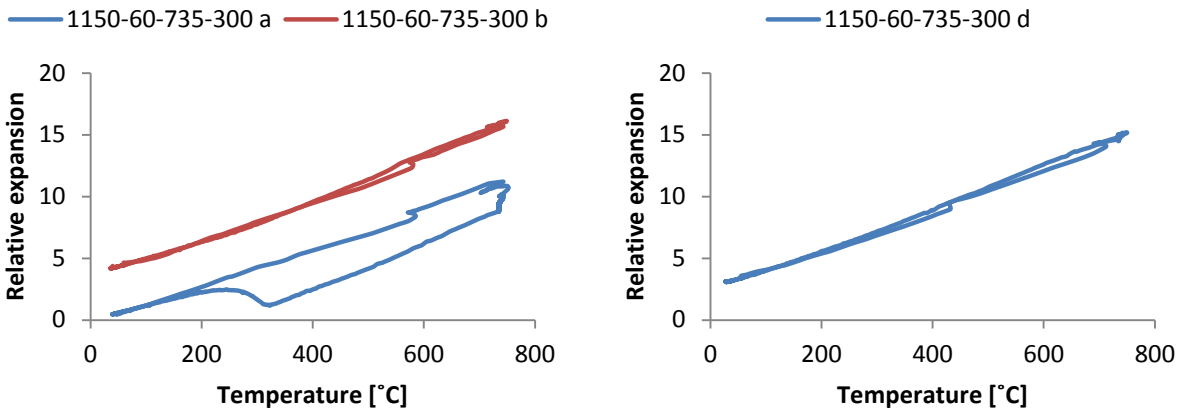

Figure 0-6: Dilatometer curves: 1150-60-735-300 a, b, d

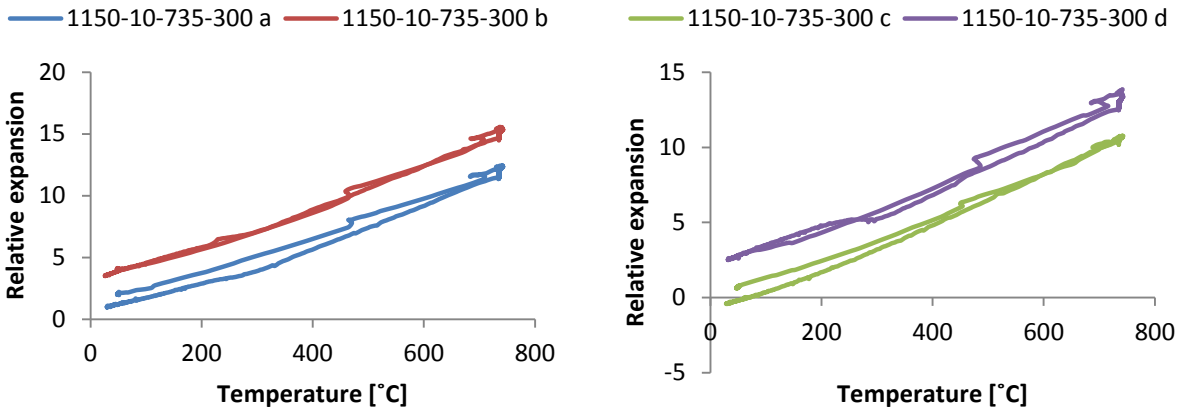

Figure 0-7: Dilatometer curves: 1150-10-735-300 a, b, c, d

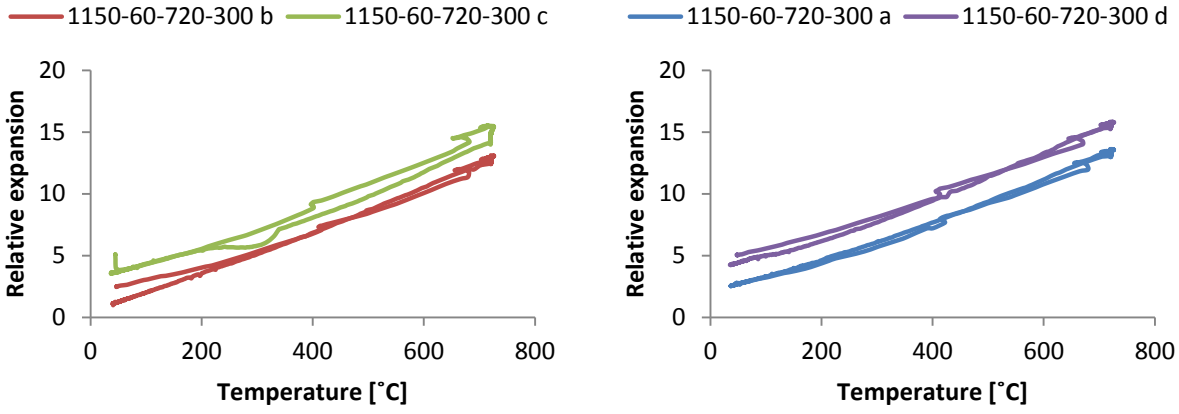

Figure 0-8: Dilatometer curves: 1150-60-720-300 a, b, c, d

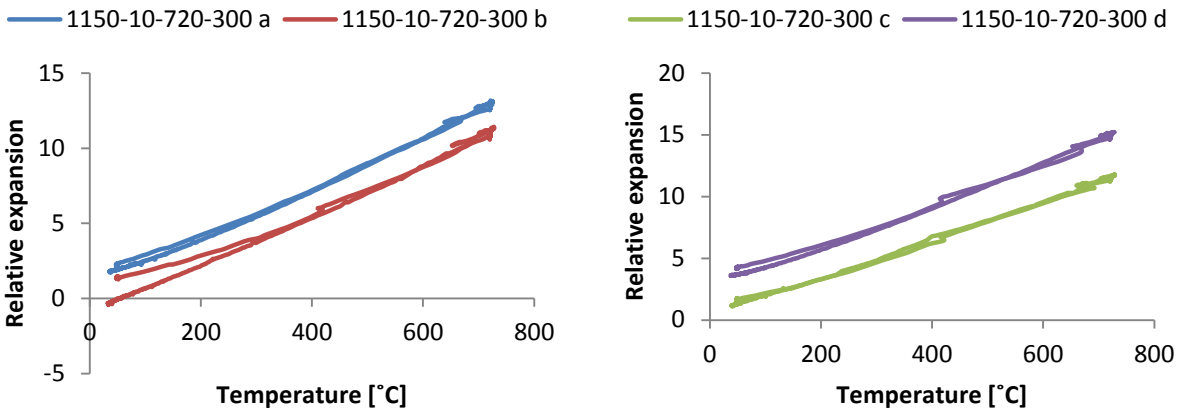

Figure 0-9: Dilatometer curves: 1150-720-300 a, b, c, d

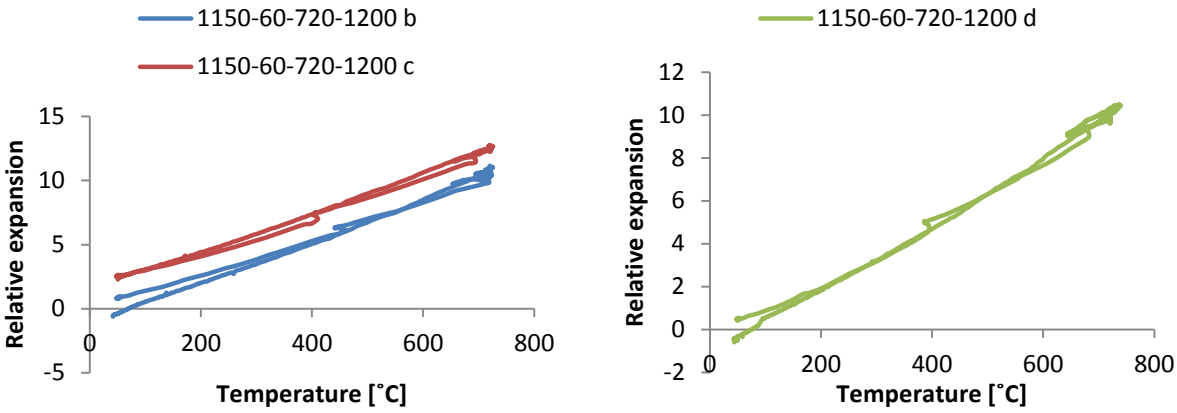

Figure 0-10: Dilatometer curves: 1150-60-720-1200 b, c, d

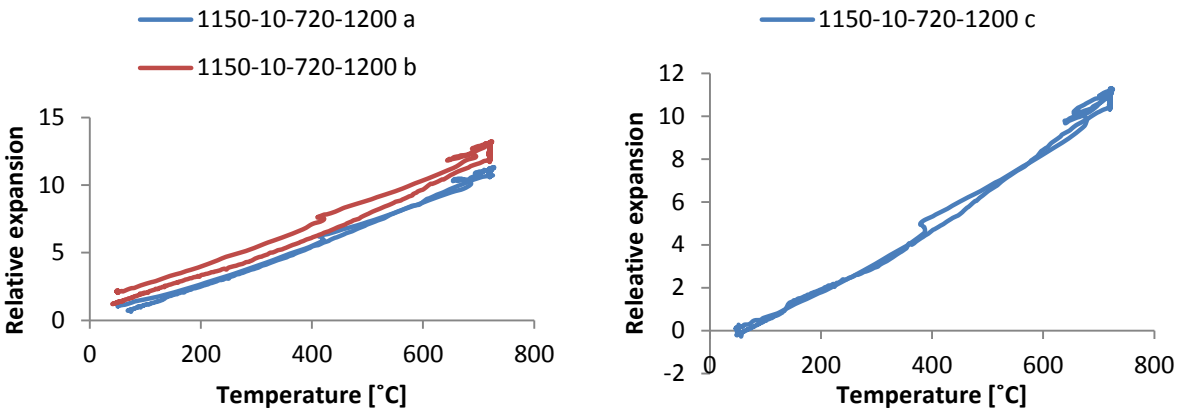

Figure 0-11: Dilatometer curves: 1150-10-720-1200 a, b, c

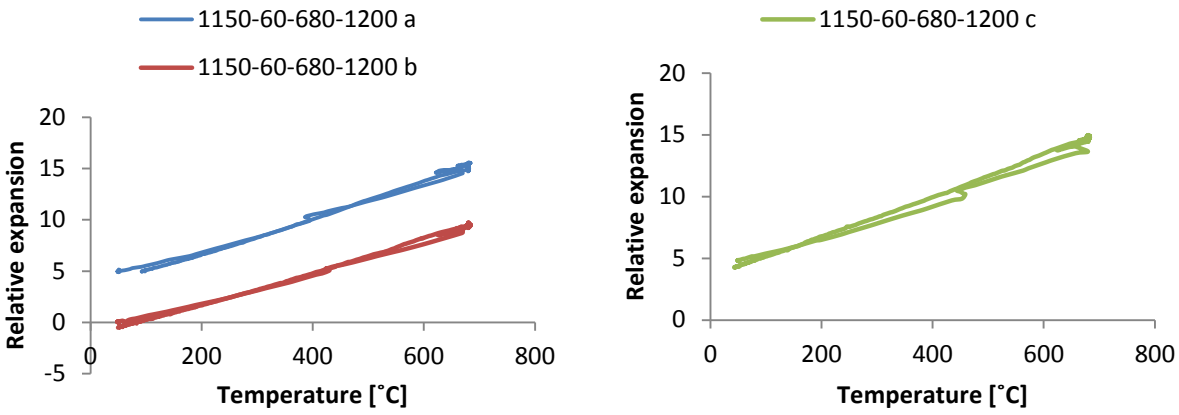

Figure 0-12: Dilatometer curves: 1150-60-680-1200 a, b, c

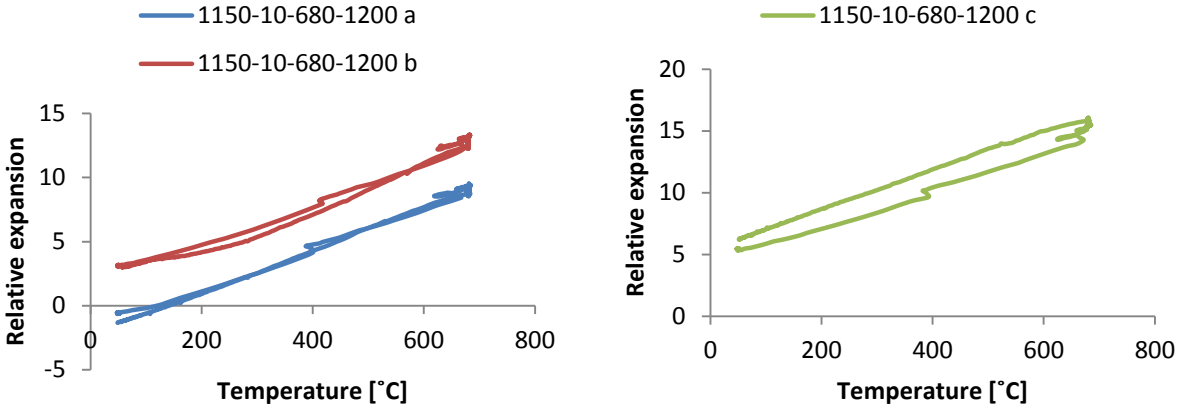

Figure 0-13: Dilatometer curves: 1150-10-680-1200 a, b, c

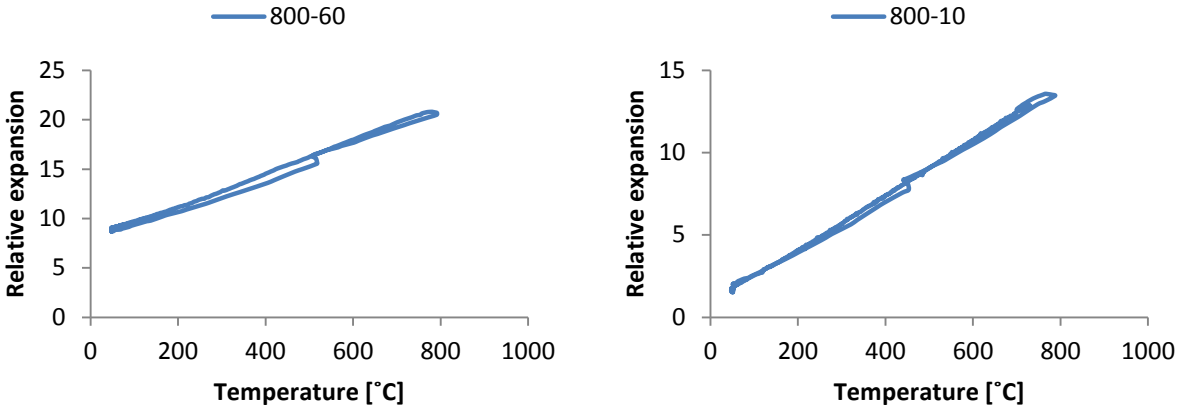

Figure 0-14: Dilatometer curves: Left: 800-10 Right: 800-10

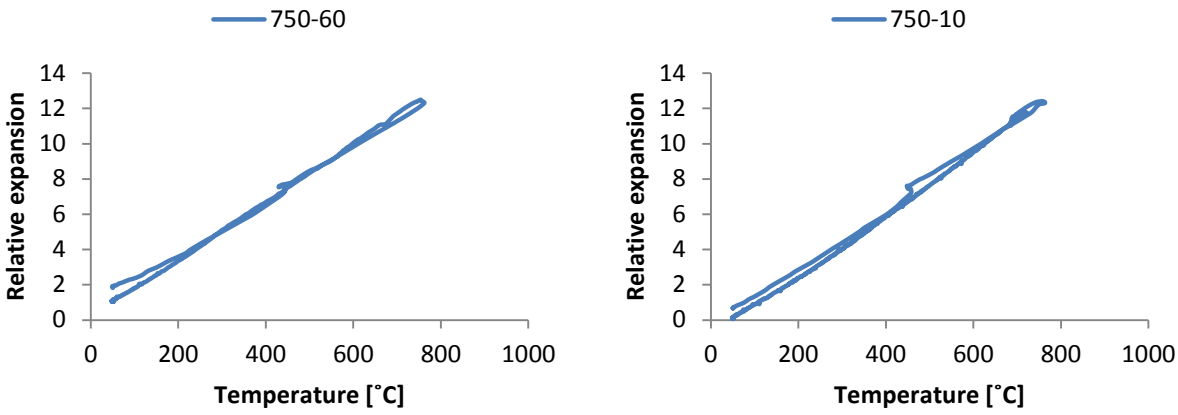

Figure 0-15: Dilatometer curves: Left: 750-60 Right: 750-10

Appendix B: Complete Charpy V chart

Table 0-1: Charpy V results.

Friction: 0,6 J	*ID*	*KV450 [J]*	*Kv450 [J] corr*	*Average*	*σ*
1150 - 60 - 735 - 300	a	32.7	32.1	34.1	9.3
	b	24.4	23.8		
	d	47	46.4		
1150 - 10 - 735 - 300	a	21.6	21	43.1	31.2
	b	21.8	21.2		
	c	87.8	87.2		
1150 - 60 - 680 - 300	a	115.5	114.9	98.2	18.2
	b	107.3	106.7		
	d	73.5	72.9		
1150 - 10 -680 -300	a	89.1	88.5	101.5	14.5
	b	94.9	94.3		
	d	122.3	121.7		
1150 - 60 - 680 - 1200	b	147.1	146.5	147.4	0.7
	c	148.9	148.3		
1150 - 10 - 680 - 1200	b	198.7	198.1	216.0	14.6
	c	234.4	233.8		
1150 - 60 - 680 - 10800	c	182.2	181.6	187.3	4.6
	d	193.5	192.9		
1150-10-680-10800	b	229.6	229	224.4	3.8
	d	220.3	219.7		
1150 - 60 - 720 - 300	a	72.5	71.9	110.6	30.1
	b	146	145.4		
	d	115	114.4		
1150 - 10 - 720 - 300	b	163.6	163	131.0	30.1
	c	91.3	90.7		
	d	140	139.4		
1150 - 60 - 720 - 1200	b	38.1	37.5	43.4	4.4
	c	45.5	44.9		
	d	48.5	47.9		
1150 - 10 - 720 - 1200	b	191.8	191.2	193.2	1.6
	c	195.8	195.2		
1150-60-720-10800	b	46.9	46.3	118.6	59.0
	d	191.4	190.8		
1150-10-720-10800	a	83.1	82.5	66.0	13.5
	b	50.1	49.5		